JGR Solid Earth

RESEARCH ARTICLE
10.1029/2023JB028525

Seismic Anisotropy and Deep Crustal Deformation Across Alaska

Chuanming Liu[1,2] **and Michael H. Ritzwoller**[2]

[1]Institute for Geophysics and Department of Earth and Planetary Sciences, Jackson School of Geosciences, The University of Texas at Austin, Austin, TX, USA, [2]Department of Physics, University of Colorado Boulder, Boulder, CO, USA

Key Points:

- A new crustal anisotropy model of Alaska is built based on a new surface wave data set and a tilted hexagonally symmetric medium assumption
- The crustal anisotropy model partitions Alaska into six distinct regions with four characteristic vertical motifs of anisotropy
- The depth variation of the tilt of anisotropy and its link to crust deformation provide new insights about Alaskan tectonics

Supporting Information:

Supporting Information may be found in the online version of this article.

Correspondence to:

C. Liu,
chuanming.liu@jsg.utexas.edu

Citation:

Liu, C., & Ritzwoller, M. H. (2024). Seismic anisotropy and deep crustal deformation across Alaska. *Journal of Geophysical Research: Solid Earth*, *129*, e2023JB028525. https://doi.org/10.1029/2023JB028525

Received 11 DEC 2023
Accepted 9 MAR 2024

Author Contributions:

Conceptualization: Chuanming Liu, Michael H. Ritzwoller
Data curation: Chuanming Liu
Formal analysis: Chuanming Liu
Funding acquisition: Michael H. Ritzwoller
Investigation: Chuanming Liu
Methodology: Chuanming Liu, Michael H. Ritzwoller
Software: Chuanming Liu
Supervision: Michael H. Ritzwoller
Validation: Chuanming Liu
Visualization: Chuanming Liu
Writing – original draft: Chuanming Liu
Writing – review & editing: Chuanming Liu, Michael H. Ritzwoller

Abstract Based on a new seismic surface wave data set, we present a model of Alaskan crustal seismic anisotropy that provides new insight into Alaska's geographically diverse deformation history. We use both Rayleigh and Love wave isotropic phase speed and Rayleigh wave azimuthal anisotropy to estimate crustal anisotropy. Unlike traditional seismic tomography, which focuses on apparent seismic anisotropy in which the symmetry axis of anisotropy is assumed to be known, we resolve the spatial variation of inherent anisotropy by inferring the depth-dependent tilt of the hexagonally symmetric elastic tensor. The amplitude of inherent anisotropy is typically stronger in the lower than the upper crust. We principally interpret the dip angle (plunge of the symmetry axis) or the tilt of the anisotropy foliation plane, which reflects the influence of vertically and/or horizontally oriented structures or deformation. The depth variation of crustal anisotropy appears in four principal motifs that partition Alaska into six distinct geographical regions, which display characteristic dip angle patterns in the upper and lower crust. By considering geological context, we discuss how each region reflects active or historical crustal deformation.

Plain Language Summary Geological observations have yielded valuable insight into the deformation history of Alaska, but the understanding of deep crustal processes remains limited. Based on seismic evidence, we present a model of seismic anisotropy that provides information about Alaska's deep crustal deformation. In contrast with most previous anisotropy studies, we focus on the tilt angle of the anisotropy foliation plane, which is caused by arbitrarily oriented structures or deformation. The resulting model partitions Alaska into six geographical regions, with four characteristic vertical tilt motifs in the upper and lower crust. We provide information about deformation in the upper and lower crust in each of these six distinct regions. By focusing on the depth variation of the tilt of anisotropy and its link to deep crustal deformation, this study complements surface geological observations and offers a new perspective on Alaskan tectonics.

1. Introduction

Alaska consists of a set of diverse tectonic terranes (Figure 1) or fault-bounded crustal blocks whose geological record is distinct from their surroundings (Colpron et al., 2007). The current collage of tectonic terranes results from multiple episodes of collision, accretion, crustal extension, rotation, delamination, strike-slip translation, and subduction (Colpron & Nelson, 2020; Coney & Jones, 1985). The Denali fault acts as a boundary that divides the state into two distinct regions with active deformation occurring primarily in southern Alaska, including the Alaska-Aleutian megathrust, due to the interaction of the Pacific plate with the North American plate (Elliott & Freymueller, 2020). Thus, current and past tectonic processes have shaped the Alaskan crust, causing crustal deformation. Deformation deep in the crust is invisible at the surface but may be revealed by observations of seismic anisotropy.

Crustal seismic anisotropy is produced by both past and present crustal deformation. Anisotropy can result from oriented cracks and fractures, the crystallographic-preferred orientation (CPO) and shape-preferred orientation (SPO) of the constituent minerals, and compositionally layered structures (Maupin & Park, 2015). Over the past two decades, surface waves have been widely applied to investigate crustal anisotropy based on observations of seismic ambient noise, which provide greater sensitivity to the crust than earthquake-derived observations because measurements extend to shorter periods (e.g., Lin et al., 2011; Moschetti et al., 2010; Shapiro & Campillo, 2004). Surface wave measurements based on continental-scale seismic arrays using new imaging methods provide a lateral resolution of about 100 km (Lin et al., 2009; Lin & Ritzwoller, 2011) and clear evidence for widespread crustal anisotropy with quantitative bounds on uncertainty (e.g., Lin et al., 2011; Xie et al., 2013).

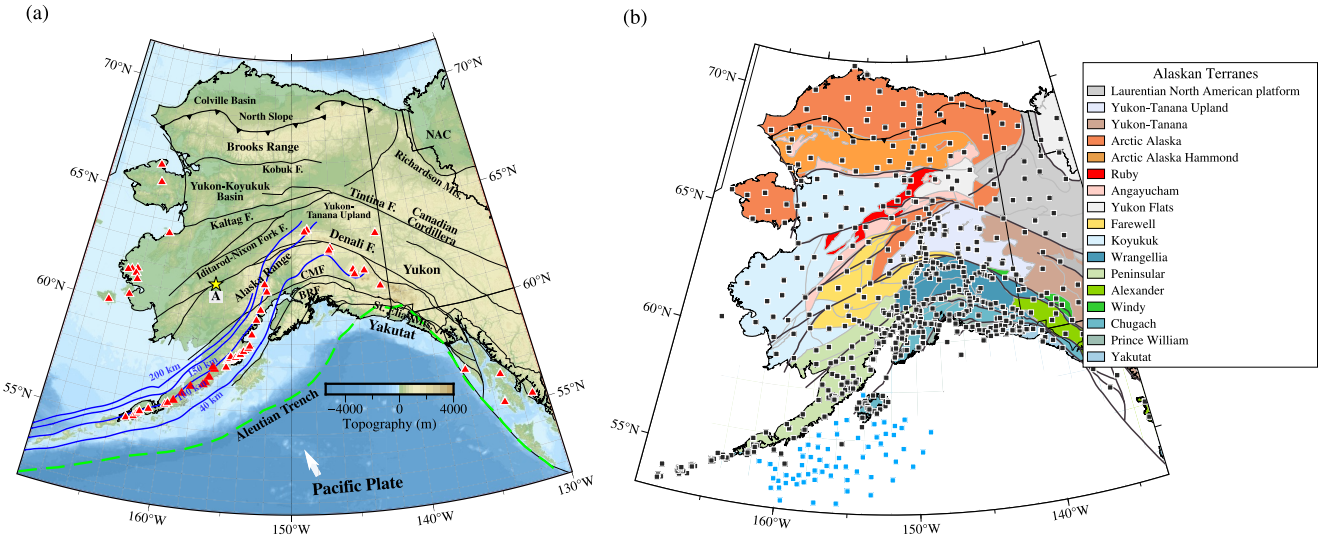

Figure 1. Alaskan faults and tectonics. (a) Topographic map of Alaska showing major faults (black curves, names ending with "F."), the depth of the subducting Pacific plate, and volcanoes (red triangles, Brueseke et al., 2023). The four blue contours show the surface of the Alaska-Aleutian subducting slab at different depths (40, 100, 150, and 200 km), based on the Slab2.0 model (Hayes et al., 2018). The white arrow indicates the direction of motion of the Pacific Plate. The green dashed line shows the plate boundary between the Pacific and North American Plates. The yellow star represents the location of an example point used in Figure 3. NAC: North American Craton. CMF: the Castle Mountain fault, BRF: the Border Ranges fault. (b) Map of tectonic terranes (Colpron et al., 2007; Colpron & Nelson, 2020) and seismic station distribution (black squares for onshore stations and blue squares for ocean bottom seismometers from the Alaska Amphibious Community Seismic Experiment).

Recent seismic studies in Alaska, based on the deployment of the USArray Transportable Array (TA) (Busby & Aderhold, 2020) and other regional seismic networks, have greatly improved the resolution of isotropic crustal structural heterogeneities (e.g., Berg et al., 2020; Chen et al., 2023; Jiang et al., 2018; Martin-Short et al., 2018; Miller & Moresi, 2018; Wang & Tape, 2014; Zhang et al., 2019). Isotropic studies provide only indirect evidence about crustal deformation. More direct information has emerged from studies of surface waves, local receiver functions and P waves, which have provided insights into the role of extensional regions, the influence of major faults on anisotropy, and mantle flow directions (e.g., Feng et al., 2020; Feng & Ritzwoller, 2019; Gou et al., 2019; Schulte-Pelkum et al., 2020). Liang et al. (2024) invert P-wave traveltime data for a model of tilted axis anisotropy focusing on the Alaskan mantle.

Most of the studies of anisotropy have been based on the inference of "apparent anisotropy" in which the orientation of anisotropy, in particular the symmetry axis, is assumed to be known. Such studies reveal neither the tilt nor the inherent strength of anisotropy. Radial anisotropy reflects the discrepancy between the speeds of horizontally and vertically polarized shear waves, while azimuthal anisotropy describes the directional dependence of surface wave speed. Strong radial anisotropy in the crystalline crust is associated with extensional deformation (e.g., Feng & Ritzwoller, 2019; Moschetti et al., 2010; Xie et al., 2013). Azimuthal anisotropy, now widely observed around the world for the continental crust (e.g., Feng et al., 2020; Lin et al., 2011; Liu et al., 2019), is generally attributed to fractures and cracks in fault zones and the CPO or SPO of crustal minerals.

For operational simplicity, most studies assume crustal anisotropy is transversely isotropic (or possesses hexagonal symmetry) with either a vertical or horizontal symmetry axis. With a vertical symmetry axis, the medium is referred to as VTI, and with a horizontal symmetry axis, it is HTI. The definition of three types of transversely isotropy is presented in Table 1. Studies of radial and azimuthal anisotropy differ in the assumed orientation of the

Table 1
Transversely Isotropic Anisotropy Types for Slow-Axis Hexagonal Medium

Abbreviation	Meaning	Corresponding observed anisotropy
VTI	Transversely isotropic medium with vertical symmetry axis	Positive radial anisotropy and no azimuthal anisotropy
HTI	Transversely isotropic medium with horizontal symmetry axis	Azimuthal anisotropy and negative radial anisotropy
TTI	Transversely isotropic medium with tilted symmetry axis	Radial anisotropy and azimuthal anisotropy

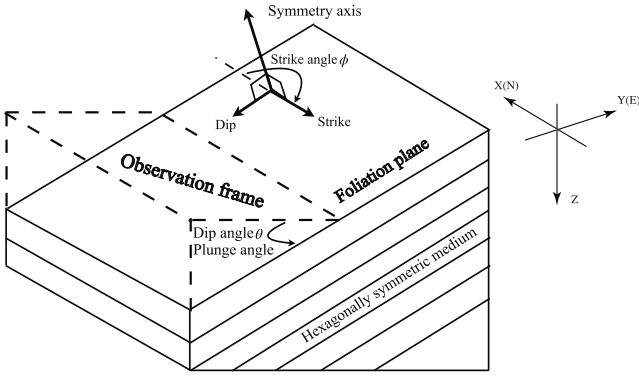

Figure 2. Depiction of the medium coordinates, aligned with the foliation plane of anisotropy. Medium coordinates are based on a tilted hexagonally symmetric elastic tensor, defined by the foliation plane (dip angle (θ) and strike angle (ϕ)).

symmetry axis. Studies of azimuthal anisotropy often assume an HTI medium with a horizontal symmetry axis and studies of radial anisotropy assume a VTI medium with a vertical symmetry axis. Positive radial anisotropy and azimuthal anisotropy are often observed to co-exist and these differing assumptions about the orientation of the symmetry axis cannot be simultaneously correct (e.g., Xie et al., 2015). This is why we refer to these studies as producing information about "apparent" anisotropy. If the symmetry axis were nearly vertical or horizontal, the anisotropy inferred would be fully accurate, but then positive radial and azimuthal anisotropy would not both exist.

Given the complexity of deformation in Alaska, it is physically unlikely that structures are oriented with a purely vertical or horizontal symmetry axis, at least across most of the region. This suggests that interpretations based on either type of apparent anisotropy not only miss information about the tilt of the elastic tensor, but they may also underestimate the amplitude of intrinsic anisotropy, may mischaracterize anisotropy, and may draw inaccurate inferences about crustal deformation. To address this issue, Xie et al. (2015, 2017) developed a new inversion method that estimates the dip angle or tilt of the anisotropy symmetry axis within the crust (Figure 2), resolving the oriented elastic tensor and accurately estimating the intrinsic strength of anisotropy. With a tilted symmetry axis and isotropy transverse to the symmetry axis, the medium is often referred to as TTI (Table 1). In this paper, we apply this innovative method to a new broadband surface wave database (Liu et al., 2022a) to estimate the observable seismic anisotropic signatures that have been imprinted on the Alaskan crust during its tectonic evolution.

This paper has two principal objectives. First, we aim to estimate crustal anisotropy using seismic surface waves and illuminate our model using geological information. Second, we seek to improve understanding of the deep expression of crustal deformation across Alaska.

The aspects of the model that we discuss here are primarily the dip angle of the foliation plane of anisotropy (Figure 2) and secondarily the inherent strength of anisotropy. Although we present the strike angle of the foliation plane of anisotropy, we do not discuss the strike angle because it has already been discussed thoroughly by Feng et al. (2020). The model we present reveals six principal regions across the state that exhibit characteristic dip angle variations with depth. Each of these regions has been affected by different tectonic processes, with different deformation histories.

The organization of the paper is as follows. In Section 2, we describe the surface wave dispersion data used in the study, the elastic moduli within a tilted hexagonally symmetric framework, and the model parameterization and constraints applied in the Bayesian Monte Carlo inversion. Section 3 presents the estimated depth-dependent dip angle and amplitude of anisotropy. In Section 4, we discuss the geological factors that contribute to crustal anisotropy and elucidate the dip angle patterns by placing them in the context of crustal deformation that is occurring or has occurred in the six distinct regions across Alaska.

2. Methods

2.1. Surface Wave Dispersion Data

We use a new database of high-resolution surface wave observations (Liu et al., 2022a) to estimate the oriented elastic tensor as a function of depth in the crust and uppermost mantle beneath Alaska. The database was constructed by employing two- and three-station ambient noise interferometry along with teleseismic earthquake data ($M_s > 5.5$) recorded at 979 broadband seismic stations (Figure 1b) across Alaska deployed from January 2000 to October 2020. Liu et al. (2022a) estimate Rayleigh and Love isotropic phase speeds, as well as Rayleigh wave phase speed anisotropy, by applying eikonal tomography for ambient noise data and Helmholtz tomography for earthquake data. The resolution of the resulting database for isotropic structure is about 80 km and for azimuthal anisotropy it is about 130 km.

The resulting data set comprises Rayleigh wave isotropic phase speed and azimuthal anisotropy at periods ranging from 8 to 85 s, as well as Love wave isotropic phase speed at periods from 8 to 80 s. All estimated quantities are

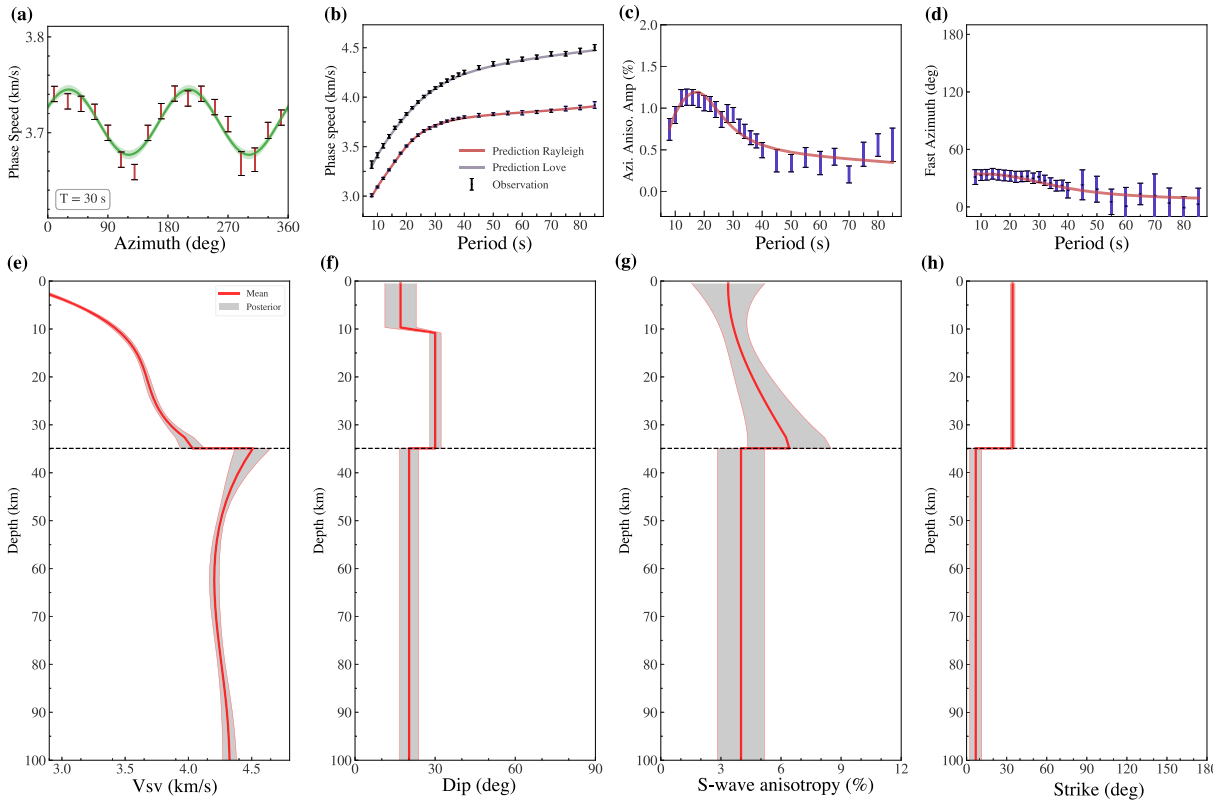

Figure 3. Examples of input surface wave local dispersion data, posterior distributions of selected model parameters, and predictions from the mean of the posterior distribution. The location of point A is in West Alaska, identified in Figure 1a. (a) Rayleigh wave phase speed measurements binned over azimuth (red bars) at 30 s period and fit for 2ψ variation (green line). (b) Rayleigh and Love wave isotropic phase speed measurements presented as one standard deviation error bars, model predictions are denoted by solid lines (Red: Rayleigh, Gray: Love). (c) The amplitude of Rayleigh wave phase speed azimuthal anisotropy measurements (blue bars) and model prediction (red line). (d) Fast azimuth of Rayleigh wave phase speed azimuthal anisotropy measurements (blue bars) and corresponding model prediction (red line) in which azimuth is defined clockwise from north. (e–h) One standard deviation extent of the posterior distribution of several model variables, shown as a function of depth where the gray corridor is two standard deviations of the posterior distribution: (e) shear wave speed (*Vsv*), (f) dip angle (θ), (g) shear wave anisotropy amplitude (γ), and (h) strike angle. The mean of each posterior distribution is shown with a red line in (e–h) and defines the model corresponding to predictions shown in (b), (c), and (d).

placed on a grid spaced at 1° in longitude and 0.5° in latitude. For each grid location at each period, the azimuthal dependence of phase speed for both Rayleigh and Love waves is parametrized as (Smith & Dahlen, 1973):

$$c(T,\psi) = c_{\text{iso}}\left[1 + A_2\cos\left(2\left(\psi - \psi_2\right)\right) + A_4\cos\left(4\left(\psi - \psi_4\right)\right)\right], \quad (1)$$

where T is period, ψ is the azimuth of propagation, c_{iso} is the isotropic phase speed, ψ_2 and ψ_4 are the fast axis orientations for the 2ψ and 4ψ components of anisotropy, and A_2 and A_4 are the relative amplitudes of the corresponding components of anisotropy. c_{iso}, A_2, A_4, ψ_2, and ψ_4 are functions of period. For the Rayleigh wave, only the 2ψ observation is used in this study, as we find the 4ψ component of anisotropy is much smaller. For the Love wave, we use only the azimuthally isotropic phase speed due to the greater difficulty in reliably estimating 4ψ anisotropy which may be as important as 2ψ anisotropy for Love waves (e.g., Montagner & Tanimoto, 1991). Estimates of all quantities and their uncertainties are presented by Liu et al. (2022a). An example of observations with uncertainty estimates is shown in Figures 3a–3d for point A identified in Figure 1a in southwestern Alaska. Figure 3a shows the azimuthal variation of Rayleigh wave phase speed at 30 s period, Figure 3b is isotropic wavespeed for Rayleigh and Love waves, Figure 3c presents the amplitude of azimuthal anisotropy A_2, and Figure 3d is the fast azimuth direction ψ_2. The fits to these data from the estimated model (e.g., red lines in Figures 3e–3h, discussed further in Section 3) are also displayed in Figures 3a–3d.

2.2. Elastic Tensor for a Tilted Transversely Anisotropic (TTI) Medium

We assume a hexagonally symmetric medium with arbitrary orientation, which is controlled by the dip angle (θ) and strike angle (ϕ) (Figure 2). When the medium possesses a vertical symmetry axis, it is classified as vertical transversely isotropic (VTI), and the elastic tensor can be expressed by five inherent elastic moduli: A, C, L, N and F (Montagner & Nataf, 1988), and summarized by the Voigt modulus matrix in abbreviated notation, $\boldsymbol{C}^{\mathrm{VTI}}$:

$$\boldsymbol{C}^{\mathrm{VTI}} = \begin{bmatrix} A & A-2N & F & 0 & 0 & 0 \\ A-2N & A & F & 0 & 0 & 0 \\ F & F & C & 0 & 0 & 0 \\ 0 & 0 & 0 & L & 0 & 0 \\ 0 & 0 & 0 & 0 & L & 0 \\ 0 & 0 & 0 & 0 & 0 & N \end{bmatrix}. \tag{2}$$

Four of the five elastic moduli are associated with the vertically and horizontally polarized S-wave velocity (V_{SV}, V_{SH}), the vertical and horizontally propagating P-wave velocity (V_{PV}, V_{PH}), and density (ρ). Parameter η is the "shape factor," which affects the elastic modulus F and characterizes the speed of wave propagation oblique to the symmetry axis. Specifically, $A = \rho V_{\mathrm{PH}}^2$, $C = \rho V_{\mathrm{PV}}^2$, $L = \rho V_{\mathrm{SV}}^2$, $N = \rho V_{\mathrm{PH}}^2$, and $F = \eta(A - 2\mathrm{L})$. In a VTI medium, there is no azimuthal anisotropy, only radial anisotropy is present, with amplitude is defined as $\gamma = \frac{N-L}{2L}$ for S-wave radial anisotropy and $\varepsilon = \frac{A-C}{2C}$ for P-wave radial anisotropy.

To determine the elastic modulus matrix, $\boldsymbol{C}^{\mathrm{TTI}}(\theta,\phi)$, for a hexagonally symmetric medium with an arbitrary orientation, we rotate the elastic modulus matrix of a VTI medium, $\boldsymbol{C}^{\mathrm{VTI}}$, though dip angle ($\theta$) and strike angle ($\phi$) using the Bond transformation matrix, $\boldsymbol{M}$, and its corresponding transpose, $\boldsymbol{M}^T$ (e.g., Auld, 1973):

$$\boldsymbol{C}^{\mathrm{TTI}}(\theta,\phi) = \boldsymbol{M}\boldsymbol{C}^{\mathrm{VTI}}\boldsymbol{M}^T, \tag{3}$$

The resulting modulus matrix can be divided into two components (Montagner & Nataf, 1988):

$$\boldsymbol{C}^{\mathrm{TTI}}(\theta,\phi)_{\mathrm{ij}} = \boldsymbol{C}_{\mathrm{ij}}^{\mathrm{EVTI}} + \delta\boldsymbol{C}_{\mathrm{ij}}, \tag{4}$$

where $\boldsymbol{C}_{\mathrm{ij}}^{\mathrm{EVTI}}$ consists of five effective vertical transversely isotropic (EVTI) moduli, $\hat{A},\hat{C},\hat{L},\hat{N}$, and $\hat{F}$, $\delta\boldsymbol{C}_{\mathrm{ij}}$ comprises parameters that describe the azimuthal anisotropy, including $G_{c,s}$,$B_{c,s}$,$H_{c,s}$, and $E_{c,s}$ (where subscripts c and s represent cosine and sine terms, respectively). The moduli, $\hat{A},\hat{C},\hat{L},\hat{N},\hat{F}$, $G_{c,s}$,$B_{c,s}$,$H_{c,s}$ and $E_{c,s}$, are defined by Equations A1–A14 in Appendix A, based on the elements of $\boldsymbol{C}^{\mathrm{TTI}}(\theta,\phi)_{ij}$.

In practice, Rayleigh and Love wave isotropic phase speeds (c_{iso}^R,c_{iso}^L) can be calculated directly based on the EVTI moduli ($\hat{A},\hat{C},\hat{L},\hat{N}$, and $\hat{F}$) or through perturbation theory (e.g., Xie et al., 2015). These expressions are related to the observed amplitude and fast direction of Rayleigh wave 2ψ azimuth anisotropy, A_2 and ψ_2, as follows:

$$A_{c,s}^R(T) = \int \left(G_{c,s}\frac{\partial c_R}{\partial \hat{L}} + B_{c,s}\frac{\partial c_R}{\partial \hat{A}} + H_{c,s}\frac{\partial c_R}{\partial \hat{F}} \right) dz, \tag{5}$$

with

$$\psi_2 = \frac{1}{2}\tan^{-1}\left(\frac{A_s^R}{A_c^R}\right), \tag{6}$$

$$A_2 = \frac{1}{2c_{\mathrm{iso}}}\sqrt{A_s^{R2} + A_c^{R2}}. \tag{7}$$

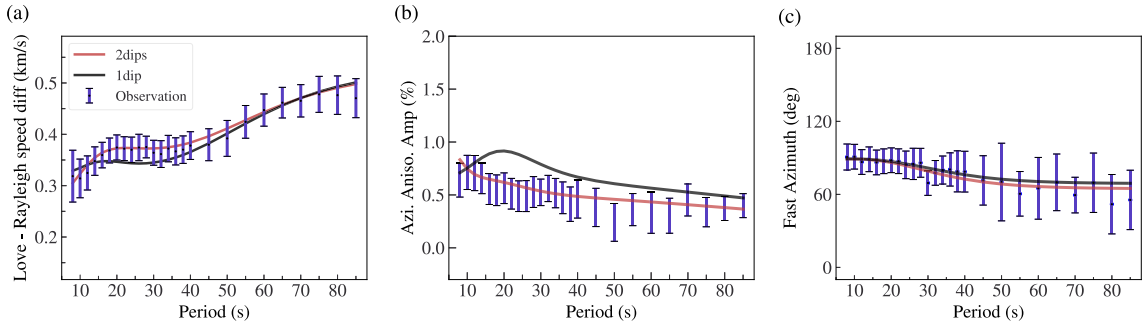

Figure 4. Example of surface wave dispersion predictions using a single dip angle with depth in the crust or two dip angles, one in the upper and one in the lower crust. Red lines are predictions with two crustal dip angles (upper crust: 65°, lower crust: 20°), black lines are predictions with a single crustal dip angle (45°). (a) Love wave and Rayleigh phase speed difference. (b) Amplitude of Rayleigh wave azimuth anisotropy. (c) Rayleigh wave fast azimuth. Constraints on the two dip angles are provided by the Rayleigh versus Love phase speed difference and the period dependence of the amplitude of azimuthal anisotropy. The location of this point is (−147° W, 63°N).

The E parameters in Equations A13 and A14 do not affect 2ψ Rayleigh wave anisotropy. We compute the partial derivatives in Equation 5 numerically, by using the transversely isotropic forward code of CPS (Herrmann, 2013).

2.3. Model Parameterization and Constraints

Our 3-D model is composed of a set of vertical 1-D models at each grid node, which we divide into three dominant depth-dependent zones: a sedimentary zone, a crystalline crustal zone, and an upper mantle zone extending from the Moho to a depth of 200 km. The sedimentary zone is isotropic except where sediment thickness is greater than 2 km, which is predominantly in the Colville Basin where the sediments are modeled as a VTI medium.

The crystalline crustal zone is considered a depth-dependent tilted hexagonally symmetric or tilted transversely isotropic (TTI) medium with seven inherent parameters: A, C, L, N, F, dip angle θ, and strike angle ϕ. A, C, N, L, and F are properties of the unrotated elastic tensor, and are considered inherent anisotropy in the frame of the foliation plane. θ and ϕ then define the rotations from the observation frame to the frame defined by the foliation plane. The depth variation of the elastic moduli A, C, L, N, and F in the crust are expressed by four B-splines. The dip angle is set to be constant in two layers within the crystalline crust, with the boundary at one-third of the crustal thickness (e.g., Xie et al., 2017). In some places, a single depth-independent dip angle would suffice to fit the data (e.g., regions with shallow/shallow or steep/steep motif of dip angle). However, in areas with shallow/steep and steep/shallow motifs of dip angle, two dip angles in the crust are needed. Figure 4 shows an example of a steep/shallow point where two dip angles are needed to fit the data. Constraints on the two dip angles are provided by the Rayleigh versus Love phase isotropic speed difference and the period dependence of the amplitude of azimuthal anisotropy. In contrast with the dip angle, we can fit the data with a constant strike angle in the crust. Figure 4c shows that at this location the fast azimuth direction changes little as a function of period and a single strike angle in the crust and another one in the mantle suffice to fit the data. The mantle is also described as a TTI medium, with the elastic moduli A, C, L, N, and F expressed with five B-splines with both dip angle and strike angle being invariant with depth in the mantle.

We use the VTI model produced by Feng and Ritzwoller (2019) as the reference model. Due to the low sensitivity of both Rayleigh and Love waves to the compressional moduli (Figure S1 in Supporting Information S1), we scale the compressional moduli (A and C) with the shear moduli (L and N) using $A = \kappa^2 N$ and $C = \kappa^2 L$, where κ is the V_P/V_S ratio ($\kappa = 1.75$ for sediment and 1.77 for the crust and mantle, following Feng and Ritzwoller (2019)). Thus, the amplitude of P-wave radial anisotropy, $\varepsilon = (A - C)/2C$, equals the amplitude of S-wave radial anisotropy, $\gamma = (N - L)/2L$.

For the TTI crust and mantle, we assume that the symmetry axis is the slow axis, which implies inherent radial anisotropy γ is positive ($N \geq L$). A slow symmetry axis is assumed because crustal structures, such as cracks and compositional layering (e.g., Crampin, 1984) and crustal rocks, can be approximated by a hexagonally symmetric medium with a slow symmetry axis (e.g., Xie et al., 2017). However, this assumption may not be appropriate for the mantle, where the hexagonal model may not have direct geological significance. Therefore, we do not interpret the mantle anisotropy in this paper.

Table 2
Prior Constraints on Model Parameters

Model parameters	Range
L at the top and bottom of the sediments	$m_0(1 \pm 0.3)$
B-spline coefficients for L within the crust and mantle	$m_0(1 \pm 0.3)$
γ within the sediments	[0, 20%]
B-spline coefficients for γ within the crust and mantle	[0, 10%]
η within the crust and mantle	[0.8, 1.1][a]
dip angle θ within the crust and mantle	[0, 90°]
strike angle ϕ within the crust and mantle	[0, 180°]

Note. m_0 is the reference model value (Feng & Ritzwoller, 2019). [a]The range is the same as Xie et al. (2017).

Sedimentary structures thinner than 2 km are isotropic with no inherent radial anisotropy, so $A = C$, $L = N$, and $F = A - 2L$ with $\eta = 1$. Sedimentary basins thicker than 2 km are parameterized as a VTI medium, with no tilting (dip $\theta = 0^{\circ}$) and no apparent azimuthal anisotropy. In the crystalline crust, A, C, L, and N (or V_{PH}, V_{PV}, V_{SH}, and V_{SV}) are constrained to increase monotonically with depth. Below 200 km depth, the mantle is set to the PREM model (Dziewonski & Anderson, 1981). Finally, density, the Q model, sedimentary thickness, and crustal thickness are fixed to the reference model of Feng and Ritzwoller (2019), which scaled density in the crust from V_{SV} and V_P using the empirical relationship of Brocher (2005) and in the mantle using the V_{SV} perturbation relative to 4.5 km/s following Hacker and Abers (2004). Shear Q in the crust is from the 1D model ak135 (Kennett et al., 1995) and in the mantle it is set to 150 similar to Shen and Ritzwoller (2016).

2.4. Bayesian Monte Carlo Inversion

In this study, we apply a Bayesian Monte Carlo inversion method to invert the data (e.g., Figures 3b–3d) at each grid node. The prior probability distributions at each grid node are defined based on the reference VTI model (Feng & Ritzwoller, 2019), and summarized in Table 2. Based on these constraints, five independent parameters (L, inherent S-wave radial anisotropy γ, dip angle θ, parameter η, and strike angle ϕ) define the model space in the Bayesian Monte Carlo inversion.

We employ a series of random walks to sample the model space guided by the prior distribution, which produces Markov Chains of candidate models. The square root of reduced chi-square misfit of a model (m) with the observation of Rayleigh and Love isotropic phase speeds and Rayleigh wave phase speed anisotropy is defined as:

$$\chi = \sqrt{\frac{1}{N}\sum_{i=1}^{N}\frac{\left[d(m)_i^{\text{pred}} - d_i^{\text{obs}}\right]^2}{\sigma_i^2}}, \tag{8}$$

where N is the number of total observations, d_i^{obs} is the observation of the datum i, $d(m)_i^{\text{pred}}$ is the prediction by the model m, and σ_i is the uncertainty of the corresponding datum i. The index i ranges over all of our data at each spatial location: Rayleigh and Love wave isotropic phase speed and the amplitude and fast axis direction of 2ψ Rayleigh wave anisotropy, all as functions of discrete period ranging from 8 to 85 s. In the model space sampling process, a model is accepted or rejected based on its likelihood function, which following Xie et al. (2015) is defined as:

$$L(m) = \exp\left(-\frac{1}{2}N\chi^2\right). \tag{9}$$

The posterior distribution is then constructed from models with misfit χ less than $\chi_{\min} + 0.5$, where $\chi_{\min}$ is the misfit value of the best-fitting model. We take as our reported model the mean of the posterior distribution as a function of depth for each of the model variables and the uncertainty, which is defined as the square root of the distribution of accepted models at each depth. An example of the prior distributions and posterior distributions is

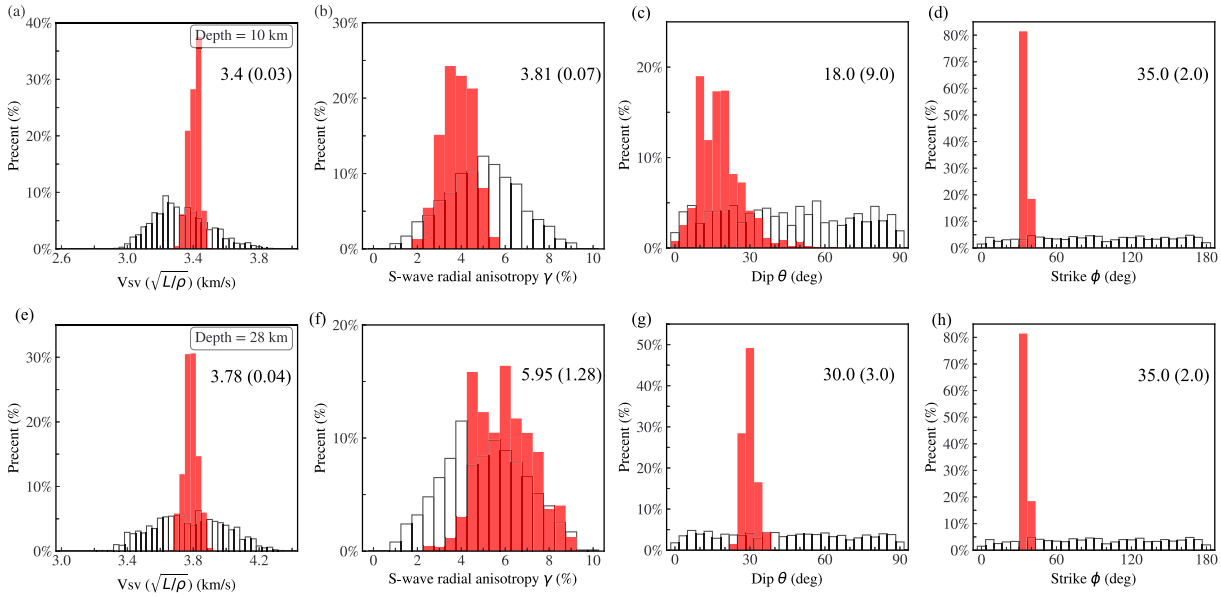

Figure 5. Examples of prior and posterior marginal distributions for five model parameters: *Vsv*, inherent S-wave anisotropy (γ), dip angle (θ), and strike angle (ϕ) at (a–d) 10 km and (e–h) 28 km depths for an example location at (157°W, 61.5°N). The white histograms are the prior marginal distributions and red histograms are the posterior marginal distributions. The mean and standard deviation of the posterior distribution are presented on each panel.

shown in Figure 5 for model variables V_{SV}, γ, θ, and ϕ. Figure S2 in Supporting Information S1 presents the map of the misfit for the reported model. The average square root of reduced chi-square misfit is smaller than 1.0.

3. Results

Based on the assumption of a tilted hexagonally symmetric or transversely isotropic (TTI) medium, we resolve the spatial variation of anisotropy represented by depth-dependent hexagonally symmetric elastic tensors using the Bayesian Monte Carlo inversion method discussed above. The elastic tensors in the upper and lower crust and uppermost mantle are defined by five unrotated elastic moduli: A, C, L, N, and F (Montagner & Nataf, 1988, see Section 2) in medium coordinates and are tilted vertically through dip angle (θ) and are horizontally aligned by strike angle (ϕ) (Figure 2) across continental Alaska on a 1°(longitude) by 0.5° (latitude) spatial grid. For a VTI medium, the elastic moduli are directly related to P- and S-wave velocity with wave propagation (V_{PH}, V_{PV}) or polarization (V_{SH}, V_{SV}) in the vertical or horizontal planes. Because we construct the elastic tensor for a VTI medium and then rotate to produce the tensor for a TTI medium, we can use these terms to describe the TTI elastic tensor, too.

Inherent radial anisotropy for S-waves in earth-centered coordinates (Figure 2) can be computed from our model and is defined as

$$\gamma = \frac{N - L}{2L}. \tag{10}$$

Details about the definitions of the elastic tensor and the model parameterization are presented in Section 2.

In a Bayesian inversion, a prior distribution of models is converted to a posterior distribution by a Markov Chain Monte Carlo sampling of model space aimed at fitting the observations. Examples of posterior distributions for several model parameters (V_{SV}, dip angle, S-wave radial anisotropy, strike angle) at Point A are shown in Figure 5. From the posterior distributions, we compute means and standard deviations of each model variable, examples of which are shown in Figures 3e–3h. In our model parametrization, V_{SV} is constrained to vary smoothly with depth in the sediments, the crystalline crust, and the mantle. Inherent radial anisotropy also varies smoothly in the crystalline crust but is constant in the mantle and zero (i.e., isotropic) in the sediments except for the Colville Basin. The strike angle is separately constant in two layers, the crystalline crust and mantle, and the

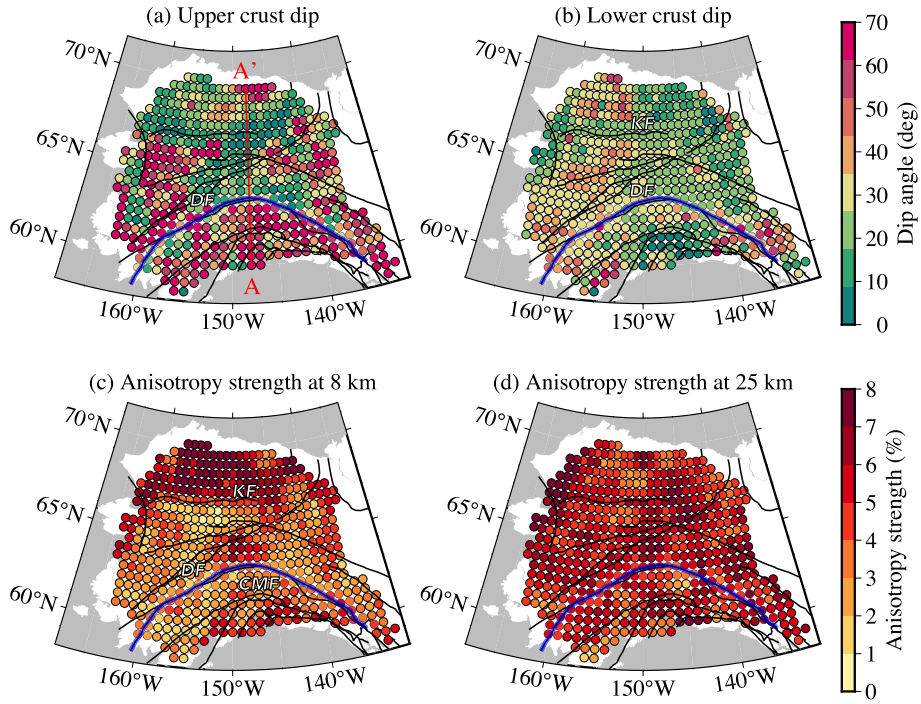

Figure 6. Surface wave anisotropy inversion results: means of the posterior distribution. Horizontal slices of dip angle (θ) in degrees in the (a) upper crust and (b) lower crust, as well as S-wave anisotropy (γ) at depths of (c) 8 km and (d) 25 km which is in the lower crust across Alaska. Major faults are shown with black lines, while the Denali fault as the major boundary is shown as a blue line. The profile AA' in (a) is used in Figure 7. DF: the Denali fault, KF: the Kobuk fault, CMF: the Castle Mountain fault.

dip angle is separately constant in three layers, the upper crust, the lower crust, and the mantle. The means of these distributions are used to generate the predictions shown in Figures 3b–3d.

We focus our discussion here predominantly on the dip angle (θ) of anisotropy, also referred to as tilt, and to a lesser extent on the strength of the inherent *S*-wave anisotropy (γ).

3.1. Dip Angle of Anisotropy

The dip angle (θ) represents the rotation of the symmetry axis from the vertical, so that $\theta = 0°$ is a vertical symmetry axis (horizontal foliation plane) and $\theta = 90°$ is a horizontal symmetry axis (see Figure 2). In the upper crust of Alaska (Figure 6a), large dip angles (>40°) are common, except for the Alaskan interior, north of the Denali fault and south of the Brooks Range, which exhibit sub-horizontal dip angles less than 20° with a sub-vertical symmetry axis. In the lower crust (Figure 6b), dip angles are commonly less than 20° in South-Central Alaska, south of the Denali fault. For Central Alaska, north of the Denali fault, there is shallow dipping in the lower crust. In contrast, lower crustal dip angles in western Alaska, southwest Yukon, and part of the North Slope are relatively large, exceeding 30°.

A north-south oriented crustal depth profile (Figure 7) along longitude 148° W across central Alaska clearly displays the contrast of dip angle between the upper and lower crust. Clear north-south variations are revealed in the dip angle, where the Denali and Kobuk faults serve as prominent east-west oriented crustal boundaries. To the south of the Denali fault, the upper crust has a steep dip angle, which overlays a sub-horizontally dipping lower crust with stronger anisotropy. In contrast, to the north of the Denali fault and south of the Brooks Range, both the upper and lower crust exhibit a small dip angle, such that the foliation plane is sub-horizontal. Additional depth profiles are shown in Figure 8.

Figure 9a presents a summary view of the depth variation of the dip angles shown in Figures 6a and 6b. The model of dip angle decomposes into four different categories depending on the steepness of the dip angle (or complementarily, the foliation plane) in the upper crust and lower crust (upper/lower) as follows: (I) shallow/

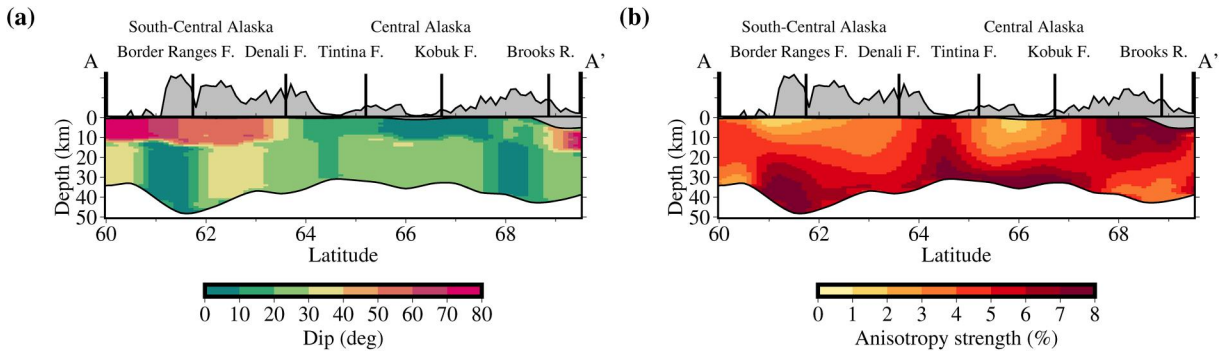

Figure 7. Surface wave anisotropy inversion results: mean of the posterior distribution. Vertical transects of (a) dip angle (θ) and (b) inherent S-wave anisotropy (γ) along the profile AA' identified in Figure 6a.

shallow, (II) steep/steep, (III) steep/shallow, and (IV) shallow/steep (Figure 9a). These categories segregate the Alaskan crust into six principal distinct regions shown in Figure 9a: (a) South-Central Alaska (SCA), which is primarily composed of the Wrangellia and Chugach terranes; (b) the Z-shaped Central Alaska (CA), encompassing the Yukon-Tanana upland, Yukon Flats, Arctic Alaska Hammond terrane, and major parts of the Ruby and Angayucham terranes; (c) West Alaska (WA), consisting of an amalgamation including the Koyukuk and parts of the Farewell terranes; (d) Southwest Yukon (SWY), including the Alexander and part of Yukon-Tanana terranes; (e) the Transition Region (TR), comprising mainly the Laurentian North American platform; and (f) the North Slope (NS), comprising mainly the Arctic Alaska terrane including the Colville Basin.

3.2. Amplitude of Anisotropy and Strike Angle

We find that anisotropy is typically stronger in the lower crust than in the upper crust. In the upper crust, relatively strong inherent S-wave anisotropy (γ), with an amplitude exceeding 5%, is concentrated beneath central Alaska, Arctic Alaska, and the South-Central Alaska in the south of the Castle Mountain fault (Figure 6c). In the lower crust, the amplitude of S-wave anisotropy is strong and nearly uniform across Alaska, with larger amplitudes compared to the upper crust except in Arctic Alaska (Figure 6d).

Clear north-south variations are also revealed in inherent strength of *S*-wave anisotropy in the depth profile, Figure 7b. To the south of the Denali fault, the upper crust has a relatively weaker inherent S-wave anisotropy, but the lower crust has a strong amplitude. Inherent *S*-wave anisotropy is strong both in the upper and lower crust in the area between the Denali and Tintina faults. To the north of the Kobuk fault, the upper crustal anisotropy is particularly strong beneath the Brooks Range and North Slope.

The strike angle (Figure 10) within the crust generally aligns with the orientation of major nearby faults. In the upper mantle, the strike angles mainly reflect the deformation and mantle flow directions near the Alaska-Aleutian subduction zone, as discussed thoroughly by Feng et al. (2020).

3.3. Uncertainty

The uncertainty for each model parameter is estimated as the standard deviation of the posterior distribution. Uncertainty maps for the dip angle and inherent strength of S-wave anisotropy are presented in Figure S3 in Supporting Information S1. For the dip angle, the average uncertainty is approximately 12° in the upper crust and 6° in the lower crust. The uncertainties in the dip angle in the lower crust are smaller because the amplitude of inherent anisotropy is larger and the lower crust tends to be thickener than the upper crust. The uncertainty in the inherent strength of *S*-wave anisotropy averages about 1% in the crust.

4. Discussion

4.1. Causes and Nature of Crustal Anisotropy

Seismic anisotropy appears almost ubiquitously in the continental crust (Almqvist & Mainprice, 2017). Unlike the horizontal orientation of the elastic tensor (strike angle) or the fast polarization direction of a surface wave, which

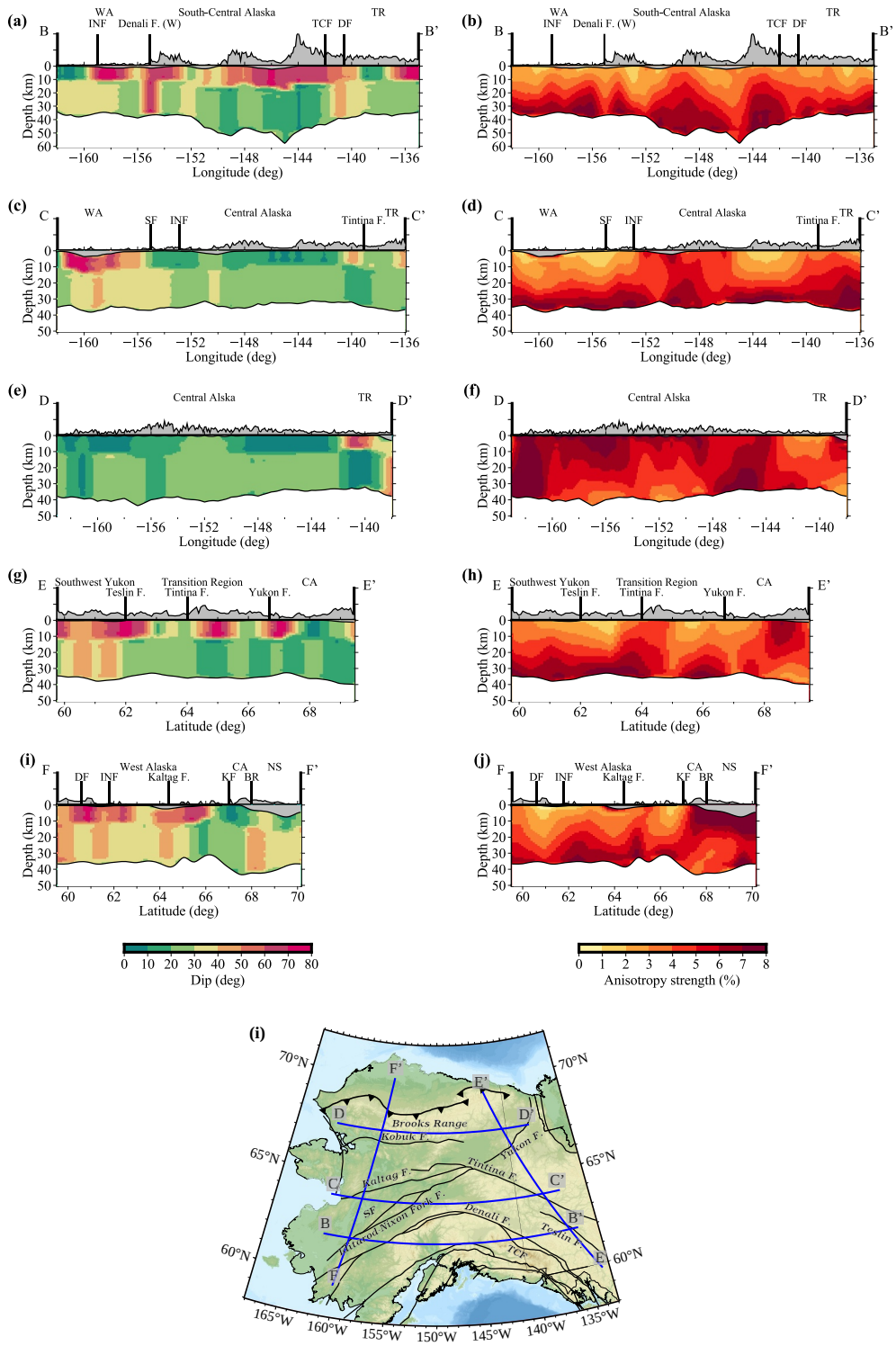

Figure 8. The same as Figure 7 but for different transects along profiles (blue lines) of BB′, CC′, DD′, EE′, and FF’ identified in (i) topography map. WA: West Alaska, TR: Transition Region, CA: Central Alaska, NS: North Slope, DF: the Denali fault, INF: the Iditarod-Nixon Fork fault, TCF: the Totschunda fault, SF: the Susulatna fault; KF: the Kobuk fault; BR: the Brooks Range.

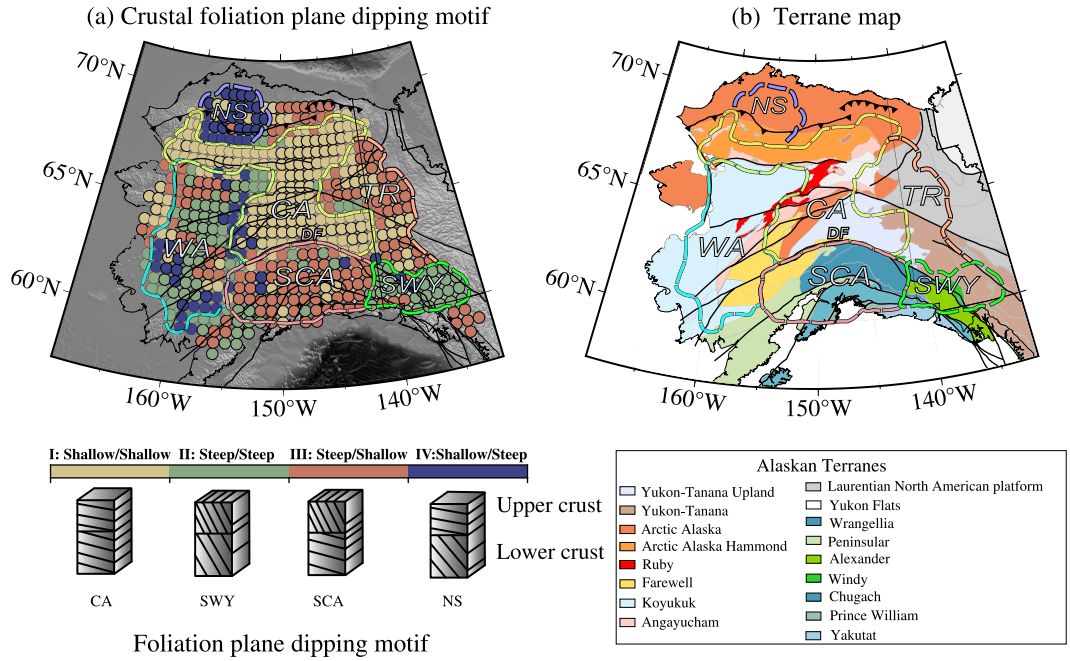

Figure 9. Crustal foliation plane orientation motif and tectonic regionalization. Foliation plane is normal to the symmetry axis. (a) The motif or category of the foliation planes is color-coded, with yellow indicating dip angles of both upper and lower crust smaller than 32°, blue indicating an upper crust dip angle less than 32° and a lower crust dip angle larger than 32°, burnt orange indicating an upper crust dip angle larger than 32° and a lower crust dip angle smaller than 32°, and green indicating dip angles across the entire crust are larger than 32°. (b) The regionalization (color-coded polygons) is defined based on the motif of crustal anisotropy, with CA representing Central Alaska, WA representing West Alaska, SCA representing South-Central Alaska, NS representing North Slope, SWY representing the Southwest Yukon, and TR representing Transition Region. DF: the Denali fault.

control the directional dependence of horizontally propagating waves, the dip angle (or tilt) of the symmetry axis of anisotropy reflects the influence of vertically and/or horizontally oriented structures or deformation.

In the continental upper crust, anisotropy is believed to be primarily controlled by stress-induced cracks (Crampin et al., 1991), macroscopically aligned fractures, and the structural fabric of rocks (Boness & Zoback, 2006; Zinke & Zoback, 2000). In addition, the crystallographic preferred orientation (CPO) of the fossil anisotropy may also be present. Due to the relatively low temperatures in the upper crust, ductile deformation and the formation of CPO may be less prevalent than in the lower crust. Upper crustal CPO may have originated in the middle to lower crust in an earlier tectonic environment (e.g., Sherrington et al., 2004). We refer to this as "fossil CPO anisotropy."

In the upper crust, a shallow dip angle is primarily associated with shallowly dipping structural fabrics (sub-horizontal bedding), such as layered sedimentary rocks or fossil CPO (Xie et al., 2013). Shallow dip angles may be linked to large-scale crustal extension, as they are in the Basin and Range Province (Johnson & Loy, 1992; Xie et al., 2015). A steep dip angle is probably caused by steeply aligned fractures or steeply dipping fossil CPO (Sherrington et al., 2004; Xie et al., 2017). For instance, in the Eastern Himalaya Syntaxis, steep upper-crustal dip angles are associated with strong clockwise deflection of the motion of the upper crust, as revealed by GPS measurements (Gan et al., 2021; Xie et al., 2017). Stress-induced cracks are another origin of upper crustal anisotropy (Crampin, 1987), with the fast polarization direction aligned with the maximum horizontal compressive stress. However, in Alaska, crustal shear wave fast directions are mostly subperpendicular to the direction of maximum horizontal stress, and are principally aligned with the orientation of major faults (Feng et al., 2020; Figure 10a). This suggests that stress-induced cracks are not a major cause of upper-crustal anisotropy in Alaska (e.g., Brocher & Christensen, 1990).

In the middle-to-lower crust, due to higher pressure and temperature, seismic anisotropy is less likely to be caused by cracks, fractures, or bedding. It is more likely to be caused by the CPO of anisotropic minerals, such as

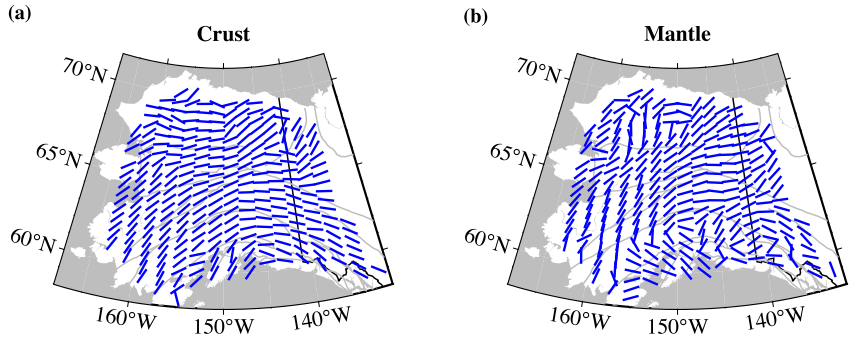

Figure 10. Map of the orientation of strike angle. The orientation is constant vertically through (a) the crust and (b) the mantle, shown with blue bars.

amphibole and mica, as well as the layering of the metamorphic and igneous rocks (e.g., Almqvist & Mainprice, 2017; Brownlee et al., 2017; Weiss et al., 1999). Ductile deformation promotes the production of CPO of anisotropic minerals (e.g., Almqvist & Mainprice, 2017). A shallow dip angle in the lower crust is associated with shallowly dipping CPO (subhorizontal foliation planes) and layered structures, which are likely caused by horizontally oriented deformations, like horizontal ductile deformation in eastern Tibet (e.g., Xie et al., 2017). Conversely, a steep dip angle in the lower crust reflects vertical deformation, which may occur due to an obstruction to horizontal deformation, such as the steep dip angles near the border of eastern Tibet being caused by the obstruction caused by the Sichuan Basin impeding middle-to-lower crustal flow (e.g., Xie et al., 2013, 2017).

To provide a simple and visually coherent distinction between the different motifs of tilt as a function of depth in the crust, we introduce four categories of anisotropy defined by the dip angle in the upper crust/lower crust. If the dip angle is greater than 32° anisotropy is considered steep, otherwise it is considered shallow. There are, therefore, four motifs of upper crust/lower crust anisotropy: Category I: shallow/shallow, Category II: steep/steep, Category III: steep/shallow, and Category IV: shallow/steep (See Table 3.). The shallow/shallow and steep/steep motifs reflect vertically coherent crustal anisotropy, whereas the vertically contrasting motifs, steep/shallow and shallow/steep, suggest a transition of anisotropy type with depth.

Category I, the shallow/shallow motif, reflects shallowly dipping structural fabrics in the upper crust, as well as shallowly dipping CPO and layered structures in the lower crust. This vertically coherent pattern of shallow dip angles may arise in an extensional tectonic setting. For example, this pattern has been identified in the Basin and Range province of the western US, where extensive extensional deformation occurs (Xie et al., 2015).

Category II, the steep/steep motif, results from a vertically oriented deformation throughout the entire crust. Macroscopically aligned subvertical fractures and the CPO of the fossil anisotropic fabric under deformation may contribute to the upper crustal anisotropy, while the CPO of anisotropic minerals would possess steeply dipping foliation planes in the lower crust. A similar motif was identified near the periphery of the eastern Tibetan Plateau, indicating strong local vertically oriented deformation in the lower crust due to the obstruction caused by the Sichuan Basin (Xie et al., 2017).

Category III, the steep/shallow motif, may result from steeply dipping aligned fractures or a steep foliation plane of anisotropic fabric in the upper crust under brittle deformation. However, a shallow dip angle in the lower crust is probably caused by the subhorizontally aligned CPO of anisotropic minerals related to ductile deformation. A similar type of anisotropy is observed in the interior of eastern Tibet, where ongoing channel flow probably occurs in the lower crust (Ozacar & Zandt, 2004; Xie et al., 2017).

Category IV, the shallow/steep motif, is the least common of the four motifs of anisotropy. It may reflect horizontal layering or exhumed sub-horizontally dipping fossil anisotropic fabric overlying a steeply dipping fossil anisotropic fabric. This category of anisotropy occurs only in geographically isolated locations in Alaska.

4.2. Regionalization of Anisotropy Across Alaska

The tilt (dip angle) of the symmetry axis of anisotropy in the upper crust and lower crust, therefore, will result from a variety of deformation mechanisms in different tectonic environments, and the inference of deformation

Table 3
Categories of Dip Angle Motifs

Category	Depiction	Upper crust/ Lower crust	Example in Alaska	Example in other places
I		Shallow/Shallow	Central Alaska	Basin and Range province
II		Steep/Steep	Southwest Yukon	Periphery of the eastern Tibetan Plateau
III		Steep/Shallow	South-Central Alaska	Interior of eastern Tibet
IV		Shallow/Steep	North Slope	–

mechanism from anisotropy is non-unique. The analysis of dip angles is best performed in concert with prior information about the geological and tectonic setting. In this context, anisotropy provides new information predominantly about the deeper crust. Here, we discuss the six regions with distinct, geographically coherent motifs of anisotropy present in Figure 6a and invoke geological, tectonic, and geodetic information to illuminate the interpretation.

4.2.1. South-Central Alaska

South-Central Alaska is a highly active tectonic environment, characterized by oblique convergence, accretion, rotation, flat subduction, and faulting (e.g., Elliott & Freymueller, 2020; Plafker et al., 1994; Redfield et al., 2007). This region contains the Wrangellia terrane, the Chugach terrane, and parts of the Peninsular and Farewell terranes, which are geographically isolated from Central and West Alaska by the Denali fault and the Alaska Range, respectively (Figure 9b). The Denali fault is an active intracontinental right-lateral strike-slip fault, which accommodates a fraction of the oblique collision of the Yakutat block with southern Alaska (Plafker et al., 1994). The neotectonics of South-Central Alaska are characterized by a wide zone of right-transpressional deformation across the Alaska Range to the north and in the Cook Inlet region to the south (Haeussler, 2008).

South-Central Alaska is nearly homogeneously composed of anisotropy Category III (Figure 9a), the steep/shallow motif, where there is a steeply dipping foliation plane in the upper crust overlying a sub-horizontal foliation plane in the lower crust. The amplitude of inherent radial anisotropy is relatively weak in the northern part of this region within the upper crust and is strong throughout the majority of the lower crust (Figure 7b).

In the upper crust, macroscopic fractures have developed due to large strike-slip and transpressional deformation (Pavlis et al., 2003), resulting in predominantly vertical foliation planes (Savage, 1999), which are reflected in steep dip angles in our model. The geological evidence, including recent past (<25 Ma) and synchronous exhumation of the Denali fault and regions south of it (Benowitz et al., 2014), plus deformation of Pliocene strata, indicate the upper crust of South-Central Alaska is quasi-rigid (Haeussler, 2008). The widespread seismicity (Figure S4 in Supporting Information S1) and strike-slip faults in the upper crust (e.g., Daly et al., 2021; Silwal et al., 2018) also point to brittle deformation. A seismic receiver function study (Schulte-Pelkum et al., 2020) found strong anisotropy at shallow depths linked to brittle fractures. Our model corroborates the existing

geological evidence that brittle deformation dominates in the upper crust and faults and fractures are the most likely source of anisotropy.

In the lower crust, seismicity is generally sparse in this region, except in the area close to subduction near the region's southern edge (e.g., Silwal et al., 2018). The temperature in the lower crust is probably elevated due to shear heating caused by the subduction of Yakutat (Finzel et al., 2014), promoting lower viscosity in the lower crust, consistent with geodetic analyses of lithospheric viscosity (Finzel et al., 2015). Our model of a sub-horizontally dipping foliation plane in the lower crust in this region is consistent with this evidence and extends it by suggesting the development of ductile deformation and horizontal extrusion. The lower crust can accommodate the large-scale rotational deflection and transpression via ductile deformation, which is analogous to the crustal channel flow hypothesized for the Tibet Plateau (Clark & Royden, 2000).

Our model suggests vertically incoherent deformation in the crust of South-Central Alaska, with brittle deformation dominating the upper crust and ductile deformation dominant in the lower crust influenced by the ongoing flat subduction of the Yakutat block, which was initiated by 30 Ma (Brueseke et al., 2019). This is consistent with known geological and tectonic information about deformation in this region and provides new evidence regarding the transition from brittle to ductile deformation within the crust throughout this region. We expect that large-scale steep/shallow motifs of crustal anisotropy may develop in analogous regions undergoing strong horizontal deflection and/or extrusional deformation, such as Anatolia (Redfield, et al., 2007).

4.2.2. Central Alaska

Central Alaska includes the Arctic Alaska Hammond subterrane, the Yukon Flats, the Yukon-Tanana upland, and the majority of the Ruby and Angayucham terranes (Figure 9b). The region is bounded to the north by the Brooks Range and to the south by the Denali fault, respectively. Within Central Alaska, the Tintina fault, a significant strike-slip fault, transects the area. Presently, Central Alaska exhibits very small GPS velocity and block motion (Elliott & Freymueller, 2020). Earthquake mechanisms observed in the south of the region reflect major strike-slip deformation. A geodetic study suggests that the crustal deformation in this area may be attributed to mantle traction (e.g., Finzel et al., 2015).

Central Alaska is nearly exclusively anisotropy Category I (Figure 9a), the shallow/shallow motif of dip angle, which manifests geographically as a distinctive “Z-shaped” pattern that defines the region. Additionally, there is strong inherent radial anisotropy, especially within the lower crust (Figure 7b).

Central Alaska experienced significant extensional deformation in the mid-Cretaceous (Hansen & Dusel-Bacon, 1998; Miller & Hudson, 1991; Pavlis et al., 1993), which generally coincident with the Z-shaped region of our model (Figure 9a). Evidence for extensional deformation in the region includes simultaneous development of depositional basins (e.g., Yukon Flats), the presence of regional normal faults, widespread shallowly dipping metamorphic foliations, penetrative extensional features within the fabric of metamorphic rocks, and the anomalously thin crust in Central Alaska. (e.g., Miller & Hudson, 1991; Moore & Box, 2016; O'Brien et al., 2018; Zhang et al., 2019). The shallow dip angles in the upper crust of our model are particularly consistent with the shallowly dipping exhumed fossil anisotropic fabrics and the layered sedimentary and metamorphic structures developed across the region.

In the lower crust, laterally homogeneous structures below 5 km depth have been revealed by the TACT project (Trans-Alaska Crustal Transect; Fuis et al., 2008), which utilized deep refraction and wide-angle reflection along the trans-Alaska oil pipeline. The study inferred widespread intrusive or metamorphic low-angle layering in Central Alaska. The shallow lower crustal dip angles in our model are consistent with the TACT profile and extend the result across the entirety of Central Alaska. Deformation is vertically coherent across the entire crust with extensional features across all of Central Alaska. The shallow/shallow motif of dip angle also has been found in the Basin and Range province, also reflecting extensional deformation (Xie et al., 2015).

Prior to the mid-Cretaceous extensional deformation, Central Alaska was recognized as part of a Jurassic contractional orogen. (e.g., Hansen & Dusel-Bacon, 1998; Moore & Box, 2016; Pavlis et al., 1993). However, our model coheres with the features associated with extensional deformation (e.g., subhorizontal foliation planes). Thus, seismic anisotropy in the Z-shaped region resulted from mid-Cretaceous extensional deformation that overprinted previous signatures of contractional deformation in Central Alaska.

4.3. West Alaska

West Alaska consists primarily of the Koyukuk terrane and portions of the Farewell, Angayucham, and Ruby terranes (Figure 9b). The Kobuk fault delineates its northern boundary. West Alaska is currently a stable block with slow westward translation, low intraregional deformation, and low seismicity rates (Elliott & Freymueller, 2020). As an exotic block relative to ancestral North America, West Alaska has experienced recurrent volcanism throughout Mesozoic and Cenozoic times (Patton, 1973; O'Brien et al., 2018), which is believed to have occurred in an ancient subduction zone (Moore & Box, 2016; Patton, 1973).

The anisotropy in West Alaska (WA) is less homogeneous than in South-Central Alaska or Central Alaska. The majority of the region falls under Category II (steep/steep), although locations near its periphery are in Category IV (shallow/steep) and also show some Category III (steep/shallow) characteristics (Figure 9a). The upper crust has weak inherent radial anisotropy, but inherent anisotropy is stronger in the lower crust (Figures 6c–6d).

In the upper crust of West Alaska, there is geological evidence for contractional deformation characterized by the thick-skinned fold and thin-skinned thrust styles during the Cretaceous period (Moore & Box, 2016). This area is roughly coincident with the region displaying steep upper crustal dip angles in the interior of West Alaska (Figure 9a, green tiles). Near the region's periphery, shallow dip angle folds and layered sedimentary rocks are observed (Moore & Box, 2016; Patton, 1973), which explains the shallow dip angles in our model in these areas (Figure 9a, blue tiles). Our model extends geological observations by indicating horizontal layering of the shallow crust near the region's periphery, which reflects less deformed layering in the post-terrane basins in this region.

Concerning the lower crust, aeromagnetic profiles exhibit pronounced anomalies over the Yukon-Koyukuk basin in West Alaska, suggesting preserved massive volcanics (Patton, 1973). Petrology and geochemistry studies have identified intrusive rocks and granitic plutons that bear characteristics of oceanic plate subduction and convergent tectonism (Box & Patton, 1989; O'Brien et al., 2018; Moore et al., 2015). The moderately steep lower crustal dip angles in our model point to an inclined fossil CPO that formed under contractional deformation in this region.

The mosaic of anisotropy categories we observe in West Alaska reflects the complex history of the emplacement and accretion of the exotic terranes onto the continent in contractional environments.

4.3.1. North Slope

The North Slope is primarily in the Arctic Alaska terrane and includes the western part of the Colville Basin and the northwest margin of the Brooks Range (Figure 9b). This region is an inactive block, characterized by minimal translation and an absence of seismicity (Elliott & Freymueller, 2020). However, in and following the Late Jurassic, Arctic Alaska was a zone of active deformation. During the Late Jurassic and earliest Cretaceous periods, the Brooks Range resulted from an arc-continent collisional orogen. North of the Brooks Range, the thick foreland basin, the Colville Basin, developed at the same period, which underwent contractional deformation during the Cenozoic period (e.g., Moore & Box, 2016; Moore et al., 1994). In contrast, the Southern Brooks Range experienced an immense degree of extensional deformation beginning ~115 Ma ago (e.g., Hoiland et al., 2018).

The North Slope (NS) of Alaska is predominantly anisotropy Category IV (Figure 9a), with a shallow/steep motif of dip angles. The upper crust in this region exhibits strong inherent radial anisotropy (Figure 6c).

In the upper crust to a depth of about 10 km, seismic reflection profiles have identified near horizontal stratification (Cole et al., 1997; Grantz et al., 1994) and surface wave studies have revealed slow shear-wave speeds (e.g., Feng & Ritzwoller, 2019). The shallow dip angles observed in the upper crust are caused by shallowly dipping sedimentary rocks deposited over time (Moore et al., 2015), and may suggest extension. In the lower crust, the steep dip angles signify vertical deformation, presumably caused by older contractional tectonism, which produced widespread thrust folds (Grantz et al., 1994; Moore & Box, 2016).

Our model of nearly homogenous Category IV anisotropy across the western Colville Basin and the northern margin of the Brooks Range is consistent with the long history of sedimentation derived from the evolution of the orogenic belt in the upper crust. In addition, due to the currently inactive tectonic environment, our model demarcates the zone exhibiting inherited, historical contractional deformation in the lower crust, separating the passive continental margin of Arctic Alaska from the interior of Alaska. Furthermore, the Brooks Range serves as a significant delineation between the region of inherited lower crustal contractional deformation in Arctic Alaska and the region of inherited extensional deformation in the Brooks Range and Central Alaska.

4.3.2. Southwest Yukon

Southwest Yukon is located in the southeastern portion of the study region, north of the Yakutat microplate. It encompasses the Alexander terrane and part of the Yukon-Tanana terrane (Figure 9b). The eastern Denali fault transverses Southwest Yukon, while the St. Elias orogen borders the region's southern margin. Significant crustal deformation has occurred in the region due to the collision and underthrusting of the Yakutat block (Ferris et al., 2003). The Yakutat block is presently moving northward at a speed of ∼50 mm/yr relative to North America (Elliott et al., 2013), which results in fault development, intense local seismicity, and the rapid rise of the St. Elias Mountains and the associated high elevation and steep topography.

Southwest Yukon (SWY) is the predominant anisotropy Category II (Figure 9a), a steep/steep motif of dip angles. As is common across much of Alaska, the inherent radial anisotropy is relatively weak in the upper crust but strong in the lower crust (Figures 6c–6d).

A geodetic study indicates that this region is currently experiencing indentational deformation (Elliott & Freymueller, 2020) with high crustal strain rates and low lithospheric effective viscosity (McConeghy et al., 2022). The St. Elias thrust belt in the south of Southwest Yukon is a fully creeping fault that accommodates the dominant convergent block motion (Elliott & Freymueller, 2020). The concentration of earthquakes is high near the Denali fault, reflecting strike-slip and contractional deformation (Mazzotti & Hyndman, 2002). However, the seismicity rate decreases rapidly from the Denali fault north to the Yukon-Tanana terrane (Elliott & Freymueller, 2020; Mazzotti & Hyndman, 2002), signifying the blockage of the Yukon-Tanana terrane to northward deformation.

The Category II (steep/steep) anisotropy in the region correlates well with the area undergoing indentational deformation. In the upper crust, steep dip angles are probably caused by near vertical fractures and steeply dipping fabrics due to local strike-slip and contractional deformation. On the other hand, in the lower crust, steep dip angles may be attributed to the steeply dipping foliation of CPO and vertical microstructures caused by vertical deformation due to the obstruction caused by the Yukon-Tanana terrane.

Category II anisotropy is expected in regions undergoing vertical deformation due to the obstruction to horizontal deformation. It has been observed near the periphery of the eastern Tibetan Plateau, where the stable Sichuan block obstructs crustal channel flow (Xie et al., 2017). It may also be expected in the Peruvian and Pampean zones of flat slab subduction in the Andes orogen (Cobbold et al., 2007; Horton et al., 2022).

4.3.3. Transition Region

The Transition Region is composed primarily of two tectonic terranes (Laurentian North America Platform, Yukon-Tanana Intermontane) separated by the Tintina fault (Figure 9b), which transects the central part of this region. The Richardson Mountains mark its eastern boundary. GPS measurements reveal that the current-day motions of this region are slow (Elliott & Freymueller, 2020). In contrast, the seismic activity in this region is strong near the Richardson Mountains and the Tintina fault, despite its location far north of the subduction zone. The Yukon-Tanana terrane between the Tintina and the Denali faults lacks seismicity (Leonard et al., 2007; Mazzotti et al., 2008).

The Transition Region (TR) is an amalgamation of Category III (steep/shallow) and Category I anisotropy (shallow/shallow) (Figure 9a). The inherent radial anisotropy strength increases with depth (Figures 6c–6d).

Ongoing seismicity observed in the Richardson Mountains and the Tintina fault reflects mainly strike-slip and transpressive deformation in this region (Leonard et al., 2007; Mazzotti et al., 2008). Regions with strong or moderate seismic activity are largely where our model displays steep upper crustal dip angles (Category III and Category II), reflecting brittle strike-slip and transpressive deformation. In contrast, the shallowly dipping miogeoclinal sedimentary and metamorphic fabrics in this region (Lund, 2008) are co-located with our shallow upper crustal dip angles in this region. The lower crust is believed to be hot and weak in the northern Cordillera based on high local heat flow and high heat generation measurements (e.g., Hyndman, 2017; Lewis et al., 2003; Mazzotti & Hyndman, 2002). The Category III (steep/shallow) anisotropy near the Richardson Mountains and the Tintina fault reflects the transition from brittle-to-ductile deformation vertically within the crust. The nearly homogenous shallow lower crustal dip angles across the region are probably caused by the shallowly dipping CPO developed in the ductile lower crust under transpressive deformation.

Our model reveals inhomogeneous dip angle patterns in the upper crust overlying homogeneous shallow dip angles in the lower crust across the region, which signifies that geographically variable deformation processes have occurred or are occurring at the margin of Laurentian North America and the northern Cordillera. The homogeneous shallow dip angles in the lower crust across this region reflect large-scale ductile deformation beneath the northern Cordillera and surrounding areas. This is consistent with the hypothesis of potential large-scale horizontal detachment of the lower crust in the North American Cordillera (Hyndman, 2017; Mazzotti & Hyndman, 2002).

5. Conclusion

Utilizing a new surface wave dispersion database and an innovative surface wave inversion method, we present a large-scale model of crustal seismic anisotropy that sheds light on the deep expression of crustal deformation. The model, combined with local geological and geophysical information, provides new insight into Alaska's geographically diverse deformation history. Unlike traditional seismic tomography, which focuses on apparent seismic anisotropy, we resolve the spatial variation of inherent anisotropy represented by depth-dependent tilted hexagonally symmetric (TTI) elastic tensors, by inverting both Rayleigh and Love wave isotropic phase speed as well as Rayleigh wave azimuthal anisotropy. The inversion of surface wave observations for the elastic tensor and the orientation of the symmetry axis (dip angle, strike angle) provides a more physically realistic crustal model than traditional methods based on assuming either azimuthal anisotropy (HTI) or radial anisotropy (VTI).

We focus interpretation on the dip angle or tilt of the anisotropy foliation plane (or the symmetry axis), which reflects the influence of vertically and/or horizontally oriented structures or deformation, and to a lesser extent on the depth dependence of the amplitude of anisotropy. Four characteristic vertical motifs, with different dip angles in the upper and lower crust, partition Alaska into six distinct geographical regions.

Regarding the amplitude of anisotropy, the lower crust generally possesses stronger anisotropy than the upper crust. This trend is caused by stronger inherent CPO forming where active ductile deformation is taking place and in the presence of layered metamorphic structure, which are promoted in the lower crust by temperatures and pressures that are higher than in the upper crust. Exceptions occur across the North Slope and parts of South-Central Alaska, but are produced by strong sedimentary layering or accretionary deformation.

The four motifs of anisotropy are not equally represented in the Alaskan crust. 37% of the region is characterized by the shallow/shallow motif, which is predominantly found in Central Alaska. A steep/shallow motif accounts for 30% and is principally observed in South-Central Alaska and the Transition Region. 19% of the region exhibits a steep/steep motif, which primarily exists in Southwest Yukon and West Alaska. The shallow/shallow motif is the least common, found in only 13% of the region, primarily in the North Slope.

South-Central Alaska is characterized by active tectonics and exhibits a steep/shallow anisotropy motif, in which the upper crust is affected by brittle deformation and the lower crust is influenced by ductile deformation. The steep/shallow motif reflects a transition from brittle to ductile deformation within the crust influenced by subduction. Central Alaska is dominated by a shallow/shallow motif, which aligns well with geological evidence of mid-Cretaceous extension that overprinted the earlier contractional anisotropy features. West Alaska exhibits a complex mosaic of anisotropy motifs, which reflects the complex influence of ancient subduction and convergent tectonism. The North Slope is characterized by shallow/steep motif, indicating historical sedimentation from orogenic belt evolution in the upper crust and inherited contractional deformation in the lower crust. Southwest Yukon is dominated by steep/steep motif, indicating that this area is undergoing vertical deformation due to the obstruction of horizontal deformation and the influence of local strike-slip, the flat subduction of the Yakutat microplate, and the blocking of the Yukon-Tanana terrane. The Transition Region presents a combination of steep/shallow and shallow/shallow motifs; the homogeneous shallow dip angles in the lower crust across this region reflect large-scale ductile deformation beneath the northern Cordillera and the margin of Laurentian North America.

We attribute some of the observed crustal anisotropy to on-going deformation. We find that southern and eastern Alaska, including South-Central Alaska, Southeast Yukon, and the Transition Region, reflect ongoing deformation associated with the subduction of the Pacific Plate and the Yakutat microplate. In contrast, past deformation has produced the anisotropy observed in Central Alaska, West Alaska, and the North Slope.

In the future, assimilating complementary observations, including receiver functions and Love wave azimuthal anisotropy, would help to improve the vertical resolution and further reduce non-uniqueness. In addition, our model provides a reference for full waveform simulation and inversion and the application of other methods to infer the elastic tensor.

Appendix A: Elastic Modulus Matrix

Based on Equation 4, the elastic modulus matrix $\boldsymbol{C}_{ij}^{TTI}$ after rotation can be decomposed into two components, $\boldsymbol{C}_{ij}^{EVTI}$ and $\delta\boldsymbol{C}_{ij}$, as follows:

$$\boldsymbol{C}_{ij}^{TTI} = \begin{bmatrix} C_{11} & C_{12} & C_{13} & C_{14} & C_{15} & C_{16} \\ C_{21} & C_{22} & C_{23} & C_{24} & C_{25} & C_{26} \\ C_{31} & C_{32} & C_{33} & C_{34} & C_{35} & C_{36} \\ C_{41} & C_{42} & C_{43} & C_{44} & C_{45} & C_{46} \\ C_{51} & C_{52} & C_{53} & C_{54} & C_{55} & C_{56} \\ C_{61} & C_{62} & C_{63} & C_{64} & C_{65} & C_{66} \end{bmatrix} = \begin{bmatrix} \hat{A} & \hat{A}-2\hat{N} & \hat{F} & 0 & 0 & 0 \\ \hat{A}-2\hat{N} & \hat{A} & \hat{F} & 0 & 0 & 0 \\ \hat{F} & \hat{F} & \hat{C} & 0 & 0 & 0 \\ 0 & 0 & 0 & \hat{L} & 0 & 0 \\ 0 & 0 & 0 & 0 & \hat{L} & 0 \\ 0 & 0 & 0 & 0 & 0 & \hat{N} \end{bmatrix} + \begin{bmatrix} \delta C_{11} & \delta C_{12} & \delta C_{13} & \delta C_{14} & \delta C_{15} & \delta C_{16} \\ \delta C_{21} & \delta C_{22} & \delta C_{23} & \delta C_{24} & \delta C_{25} & \delta C_{26} \\ \delta C_{31} & \delta C_{32} & \delta C_{33} & \delta C_{34} & \delta C_{35} & \delta C_{36} \\ \delta C_{41} & \delta C_{42} & \delta C_{43} & \delta C_{44} & \delta C_{45} & \delta C_{46} \\ \delta C_{51} & \delta C_{52} & \delta C_{53} & \delta C_{54} & \delta C_{55} & \delta C_{56} \\ \delta C_{61} & \delta C_{62} & \delta C_{63} & \delta C_{64} & \delta C_{65} & \delta C_{66} \end{bmatrix} \tag{A1}$$

$\boldsymbol{C}_{ij}^{EVTI}$ consists of five effective transversely isotropic (EVTI) moduli, $\hat{A},\hat{C},\hat{L},\hat{N}$, and $\hat{F}$, where

$$\hat{A} = \frac{3(C_{11}+C_{22})}{8} + \frac{C_{12}}{4} + \frac{C_{66}}{2}, \tag{A2}$$

$$\hat{C} = C_{33}, \tag{A3}$$

$$\hat{L} = \frac{C_{44}+C_{55}}{2}, \tag{A4}$$

$$\hat{N} = \frac{C_{11}+C_{22}}{8} - \frac{C_{12}}{4} + \frac{C_{66}}{2}, \tag{A5}$$

$$\hat{F} = \frac{C_{13}+C_{23}}{2}. \tag{A6}$$

$\delta\boldsymbol{C}_{ij}$ comprises parameters that describe the azimuthal anisotropy, including $G_{c,s}$,$B_{c,s}$,$H_{c,s}$, and $E_{c,s}$ (where subscripts c and s represent cosine and sine terms, respectively), with

$$G_c = \frac{C_{55}-C_{44}}{2}, \tag{A7}$$

$$G_s = C_{54}, \tag{A8}$$

$$B_c = \frac{C_{11}-C_{22}}{2}, \tag{A9}$$

$$B_s = C_{16}+C_{26}, \tag{A10}$$

$$H_c = \frac{C_{13} - C_{23}}{2}, \tag{A11}$$

$$H_s = C_{36}, \tag{A12}$$

$$E_c = \frac{C_{11} + C_{22}}{8} - \frac{C_{12}}{4} - \frac{C_{66}}{2}, \tag{A13}$$

$$E_s = \frac{C_{16} - C_{26}}{2}. \tag{A14}$$

Data Availability Statement

The composite surface wave dispersion data set can be found at Liu et al. (2022b). Original seismic waveform data were obtained from the Data Management Center of IRIS (www.iris.edu). The seismic model presented herein are available at Liu and Ritzwoller (2024), the model will also be made available at the EarthScope Earth Model Collaboration repository (https://ds.iris.edu/ds/products/emc-earthmodels/). The GMT code used to create the figures is available at www.soest.hawaii.edu/gmt.

Acknowledgments

We thank two anonymous reviewers, the associate editor, and editor, Michael Bostock, for constructive comments. We thank Jeff Benowitz, Anne Sheehan, Craig Jones, Vera Schulte-Pelkum, Kevin Mahan, Jonathan Caine, Danny Stockli, Julie Elliott, and Hersh Gilbert for valuable discussions on Alaskan geology and geophysics. We are grateful to Lili Feng, Mengyu Wu, Xiongwei Liu, and Shane Zhang for providing helpful suggestions. We greatly appreciate the community members who contributed to the data acquisition of the Alaska Transportable Array, Alaska Regional Network, AACSE, and other networks in the region. The facilities of IRIS Data Services, and specifically the IRIS Data Management Center, were used for access to waveforms, related metadata and/or derived products used in this study. IRIS Data Services are funded through the Seismological Facilities for the Advancement of Geoscience and EarthScope (SAGE) Proposal of the National Science Foundation under Cooperative Agreement EAR-1851048. This study was funded by NSF Grants EAR-1928395 and EAR-1952209 at the University of Colorado Boulder. C. Liu was supported by the JSG Distinguished Postdoctoral Fellowship at the University of Texas at Austin.

References

Almqvist, B. S., & Mainprice, D. (2017). Seismic properties and anisotropy of the continental crust: Predictions based on mineral texture and rock microstructure: Seismic properties of the crust. *Reviews of Geophysics*, *55*(2), 367–433. https://doi.org/10.1002/2016rg000552

Auld, B. A. (1973). In *Acoustic fields and waves in solids* (Vol. I, p. 423). Wiley.

Benowitz, J. A., Layer, P. W., & Vanlaningham, S. (2014). Persistent long-term (c. 24 Ma) exhumation in the Eastern Alaska Range constrained by stacked thermochronology. *Geological Society, London, Special Publications*, *378*(1), 225–243. https://doi.org/10.1144/sp378.12

Berg, E. M., Lin, F., Allam, A., Schulte-Pelkum, V., Ward, K. M., & Shen, W. (2020). Shear velocity model of Alaska via joint inversion of Rayleigh wave ellipticity, phase velocities, and receiver functions across the Alaska transportable array. *Journal of Geophysical Research: Solid Earth*, *125*(2). https://doi.org/10.1029/2019jb018582

Boness, N. L., & Zoback, M. D. (2006). Mapping stress and structurally controlled crustal shear velocity anisotropy in California. *Geology*, *34*(10), 825–828. https://doi.org/10.1130/g22309.1

Box, S. E., & Patton, W. W. (1989). Igneous history of the Koyukuk Terrane, western Alaska: Constraints on the origin, evolution, and ultimate collision of an accreted island arc terrane. *Journal of Geophysical Research*, *94*(B11), 15843–15867. https://doi.org/10.1029/jb094ib11p15843

Brocher, T. M. (2005). Empirical relations between elastic wave speeds and density in the Earth's crust. *Bulletin of the Seismological Society of America*, *95*(6), 2081–2092. https://doi.org/10.1785/0120050077

Brocher, T. M., & Christensen, N. I. (1990). Seismic anisotropy due to preferred mineral orientation observed in shallow crustal rocks in southern Alaska. *Geology*, *18*(8), 737–740. https://doi.org/10.1130/0091-7613(1990)018

Brownlee, S. J., Schulte-Pelkum, V., Raju, A., Mahan, K., Condit, C., & Orlandini, O. F. (2017). Characteristics of deep crustal seismic anisotropy from a compilation of rock elasticity tensors and their expression in receiver functions. *Tectonics*, *36*(9), 1835–1857. https://doi.org/10.1002/2017tc004625

Brueseke, M. E., Benowitz, J. A., Bearden, A. T., Mann, M. E., & Miggins, D. P. (2023). Subduction disruption, slab tears: Ca. 1 Ma true collision of an ~30-km-thick oceanic plateau segment recorded by Yakutat slab nascent tear magmatism. *Terra Nova*, *35*(1), 49–57. https://doi.org/10.1111/ter.12628

Brueseke, M. E., Benowitz, J. A., Trop, J. M., Davis, K. N., Berkelhammer, S. E., Layer, P. W., & Morter, B. K. (2019). The Alaska Wrangell arc: ~30 Ma of subduction-related magmatism along a still active arc-transform junction. *Terra Nova*, *31*(1), 59–66. https://doi.org/10.1111/ter.12369

Busby, R. W., & Aderhold, K. (2020). The Alaska transportable array: As built. *Seismological Research Letters*, *91*(6), 3017–3027. https://doi.org/10.1785/0220200154

Chen, G., Chen, J., Tape, C., Wu, H., & Tong, P. (2023). Double-difference adjoint tomography of the crust and uppermost mantle beneath Alaska. *Journal of Geophysical Research: Solid Earth*, *128*(1). https://doi.org/10.1029/2022jb025168

Clark, M. K., & Royden, L. H. (2000). Topographic ooze: Building the eastern margin of Tibet by lower crustal flow. *Geology*, *28*(8), 703–706. https://doi.org/10.1130/0091-7613(2000)28

Cobbold, P. R., Rossello, E. A., Roperch, P., Arriagada, C., Gómez, L. A., & Lima, C. (2007). Distribution, timing, and causes of Andean deformation across South America. *Geological Society, London, Special Publications*, *272*(1), 321–343. https://doi.org/10.1144/gsl.sp.2007.272.01.17

Cole, F., Bird, K. J., Toro, J., Roure, F., O'Sullivan, P. B., Pawlewicz, M., & Howelll, D. G. (1997). An integrated model for the tectonic development of the frontal Brooks range and Colville Basin 250 km west of the trans-Alaska crustal transect. *Journal of Geophysical Research*, *102*(B9), 20685–20708. https://doi.org/10.1029/96jb03670

Colpron, M., & Nelson, J. L. (2020). Reference module in Earth systems and environmental sciences (Geosphere 10 2014). https://doi.org/10.1016/b978-0-12-409548-9.12502-3

Colpron, M., Nelson, J. L., & Murphy, D. C. (2007). Northern Cordilleran terranes and their interactions through time. *Geological Society of America Today*, *17*(4), 4. https://doi.org/10.1130/gsat01704-5a.1

Coney, P. J., & Jones, D. L. (1985). Accretion tectonics and crustal structure in Alaska. *Tectonophysics*, *119*(1–4), 265–283. https://doi.org/10.1016/0040-1951(85)90042-3

Crampin, S. (1984). Effective anisotropic elastic constants for wave propagation through cracked solids. *Geophysical Journal of the Royal Astronomical Society*, *76*(1), 135–145. https://doi.org/10.1111/j.1365-246x.1984.tb05029.x

Crampin, S. (1987). Geological and industrial implications of extensive-dilatancy anisotropy. *Nature*, *328*(6130), 491–496. https://doi.org/10.1038/328491a0

Crampin, S., Brocher, T. M., & Christensen, N. I. (1991). Comment and Reply on Seismic anisotropy due to preferred mineral orientation observed in shallow crustal rocks in southern Alaska. *Geology*, *19*(8), 859–860. https://doi.org/10.1130/0091-7613(1991)019

Daly, K. A., Abers, G. A., Mann, M. E., Roecker, S., & Christensen, D. H. (2021). Subduction of an oceanic plateau across Southcentral Alaska: High-resolution seismicity. *Journal of Geophysical Research: Solid Earth*, *126*(11). https://doi.org/10.1029/2021jb022809

Dziewonski, A. M., & Anderson, D. L. (1981). Preliminary reference Earth model. *Physics of the Earth and Planetary Interiors*, *25*(4), 297–356. https://doi.org/10.1016/0031-9201(81)90046-7

Elliott, J., & Freymueller, J. T. (2020). A block model of present-day Kinematics of Alaska and Western Canada. *Journal of Geophysical Research: Solid Earth*, *125*(7). https://doi.org/10.1029/2019jb018378

Elliott, J., Freymueller, J. T., & Larsen, C. F. (2013). Active tectonics of the St. Elias orogen, Alaska, observed with GPS measurements. *Journal of Geophysical Research: Solid Earth*, *118*(10), 5625–5642. https://doi.org/10.1002/jgrb.50341

Feng, L., Liu, C., & Ritzwoller, M. H. (2020). Azimuthal anisotropy of the crust and uppermost mantle beneath Alaska. *Journal of Geophysical Research: Solid Earth*, *125*(12). https://doi.org/10.1029/2020jb020076

Feng, L., & Ritzwoller, M. H. (2019). A 3-D shear velocity model of the crust and uppermost mantle beneath Alaska including apparent radial anisotropy. *Journal of Geophysical Research: Solid Earth*, *124*(10), 10468–10497. https://doi.org/10.1029/2019jb018122

Ferris, A., Abers, G. A., Christensen, D. H., & Veenstra, E. (2003). High resolution image of the subducted Pacific (?) plate beneath central Alaska, 50-150 km depth. *Earth and Planetary Science Letters*, *214*(3-4), 575–588. https://doi.org/10.1016/S0012-821X(03)00403-5

Finzel, E. S., Flesch, L. M., & Ridgway, K. D. (2014). Present-day geodynamics of the northern north American Cordillera. *Earth and Planetary Science Letters*, *404*, 111–123. https://doi.org/10.1016/j.epsl.2014.07.024

Finzel, E. S., Flesch, L. M., Ridgway, K. D., Holt, W. E., & Ghosh, A. (2015). Surface motions and intraplate continental deformation in Alaska driven by mantle flow. *Geophysical Research Letters*, *42*(11), 4350–4358. https://doi.org/10.1002/2015gl063987

Fuis, G. S., Moore, T. E., Plafker, G., Brocher, T. M., Fisher, M. A., Mooney, W. D., et al. (2008). Trans-Alaska Crustal Transect and continental evolution involving subduction underplating and synchronous foreland thrusting. *Geology*, *36*(3), 267–270. https://doi.org/10.1130/g24257a.1

Gan, W., Molnar, P., Zhang, P., Xiao, G., Liang, S., Zhang, K., et al. (2021). Initiation of clockwise rotation and Eastward Transport of southeastern Tibet inferred from deflected fault traces and GPS observations. *GSA Bulletin*, *134*(5–6), 1129–1142. https://doi.org/10.1130/b36069.1

Gou, T., Zhao, D., Huang, Z., & Wang, L. (2019). Aseismic deep slab and mantle flow beneath Alaska: Insight from anisotropic tomography. *Journal of Geophysical Research: Solid Earth*, *124*(2), 1700–1724. https://doi.org/10.1029/2018jb016639

Grantz, A., May, S. D., & Hart, P. E. (1994). Geology of the Arctic continental margin of Alaska (pp. 17–48). https://doi.org/10.1130/dnag-gna-g1.17

Hacker, B. R., & Abers, G. A. (2004). Subduction Factory 3: An Excel worksheet and macro for calculating the densities, seismic wave speeds, and H_2O contents of minerals and rocks at pressure and temperature. *Geochemistry, Geophysics, Geosystems*, *5*(1), Q01005. https://doi.org/10.1029/2003GC000614

Haeussler, P. J. (2008). An overview of the neotectonics of interior Alaska: Far-field deformation from the Yakutat microplate collision (pp. 83–108). https://doi.org/10.1029/179gm05

Hansen, V. L., & Dusel-Bacon, C. (1998). Structural and kinematic evolution of the Yukon-Tanana upland tectonites, east-central Alaska: A record of late Paleozoic to Mesozoic crustal assembly. *GSA Bulletin*, *110*(2), 211–230. https://doi.org/10.1130/0016-7606(1998)110

Hayes, G. P., Moore, G. L., Portner, D. E., Hearne, M., Flamme, H., Furtney, M., & Smoczyk, G. M. (2018). Slab2, a comprehensive subduction zone geometry model. *Science (New York, N.Y.)*, *362*(6410), 58–61. https://doi.org/10.1126/science.aat4723

Herrmann, R. B. (2013). Computer programs in seismology: An evolving tool for instruction and research. *Seismological Research Letters*, *84*(6), 1081–1088. https://doi.org/10.1785/0220110096

Hoiland, C. W., Miller, E. L., & Pease, V. (2018). Greenschist facies metamorphic zircon overgrowths as a constraint on exhumation of the Brooks range metamorphic core, Alaska. *Tectonics*, *37*(10), 3429–3455. https://doi.org/10.1029/2018tc005006

Horton, B. K., Capaldi, T. N., & Perez, N. D. (2022). The role of flat slab subduction, ridge subduction, and tectonic inheritance in Andean deformation. *Geology*, *50*(9), 1007–1012. https://doi.org/10.1130/g50094.1

Hyndman, R. D. (2017). Lower-crustal flow and detachment in the North American Cordillera: A consequence of Cordillera-wide high temperatures. *Geophysical Journal International*, *209*(3), 1779–1799. https://doi.org/10.1093/gji/ggx138

Jiang, C., Schmandt, B., Ward, K. M., Lin, F., & Worthington, L. L. (2018). Upper mantle seismic structure of Alaska from Rayleigh and S wave tomography. *Geophysical Research Letters*, *45*(19), 10350–10359. https://doi.org/10.1029/2018gl079406

Johnson, R. A., & Loy, K. L. (1992). Seismic reflection evidence for seismogenic low-angle faulting in southeastern Arizona. *Geology*, *20*(7), 597–600. https://doi.org/10.1130/0091-7613(1992)020

Kennett, B. L. N., Engdahl, E. R., & Buland, R. (1995). Constraints on seismic velocities in the Earth from travel times. *Geophysical Journal International*, *122*(1), 108–124. https://doi.org/10.1111/j.1365-246X.1995.tb03540.x

Leonard, L. J., Hyndman, R. D., Mazzotti, S., Nykolaishen, L., Schmidt, M., & Hippchen, S. (2007). Current deformation in the northern Canadian Cordillera inferred from GPS measurements. *Journal of Geophysical Research*, *112*(B11). https://doi.org/10.1029/2007jb005061

Lewis, T. J., Hyndman, R. D., & Flück, P. (2003). Heat flow, heat generation, and crustal temperatures in the northern Canadian Cordillera: Thermal control of tectonics. *Journal of Geophysical Research*, *108*(B6). https://doi.org/10.1029/2002jb002090

Liang, X., Zhao, D., Hua, Y., & Xu, Y. (2024). Big mantle wedge and intraplate volcanism in Alaska: Insight from anisotropic tomography. *Journal of Geophysical Research: Solid Earth*, *129*(1). https://doi.org/10.1029/2023jb027617

Lin, F., & Ritzwoller, M. H. (2011). Helmholtz surface wave tomography for isotropic and azimuthally anisotropic structure. *Geophysical Journal International*, *186*(3), 1104–1120. https://doi.org/10.1111/j.1365-246x.2011.05070.x

Lin, F., Ritzwoller, M. H., & Snieder, R. (2009). Eikonal tomography: Surface wave tomography by phase front tracking across a regional broad-band seismic array. *Geophysical Journal International*, *177*(3), 1091–1110. https://doi.org/10.1111/j.1365-246x.2009.04105.x

Lin, F., Ritzwoller, M. H., Yang, Y., Moschetti, M. P., & Fouch, M. J. (2011). Complex and variable crustal and uppermost mantle seismic anisotropy in the Western United States. *Nature Geoscience*, *4*(1), 55–61. https://doi.org/10.1038/ngeo1036

Liu, C., & Ritzwoller, M. H. (2024). Seismic anisotropy and deep crustal deformation across Alaska [Dataset]. *Zenodo*. https://doi.org/10.5281/zenodo.10723709

Liu, C., Yao, H., Yang, H., Shen, W., Fang, H., Hu, S., & Qiao, L. (2019). Direct inversion for three-dimensional shear wave speed azimuthal anisotropy based on surface wave ray tracing: Methodology and application to Yunnan, southwest China. *Journal of Geophysical Research: Solid Earth*, *124*(11), 11394–11413. https://doi.org/10.1029/2018jb016920

Liu, C., Zhang, S., Sheehan, A. F., & Ritzwoller, M. H. (2022a). Surface wave isotropic and azimuthally anisotropic dispersion across Alaska and the Alaska-Aleutian subduction zone. *Journal of Geophysical Research: Solid Earth*, *127*(11). https://doi.org/10.1029/2022jb024885

Liu, C., Zhang, S., Sheehan, A. F., & Ritzwoller, M. H. (2022b). Surface wave isotropic and azimuthally anisotropic dispersion across Alaska and the Alaska-Aleutian subduction zone [Dataset]. *Zenodo*. https://doi.org/10.5281/zenodo.7080282

Lund, K. (2008). Geometry of the Neoproterozoic and Paleozoic rift margin of Western Laurentia: Implications for mineral deposit settings. *Geosphere*, *4*(2), 429–444. https://doi.org/10.1130/ges00121.1

Martin-Short, R., Allen, R., Bastow, I. D., Porritt, R. W., & Miller, M. S. (2018). Seismic imaging of the Alaska subduction zone: Implications for slab geometry and volcanism. *Geochemistry, Geophysics, Geosystems*, *19*(11), 4541–4560. https://doi.org/10.1029/2018gc007962

Maupin, V., & Park, J. (2015). Treatise on geophysics (2nd ed., pp. 277–305). https://doi.org/10.1016/b978-0-444-53802-4.00007-5

Mazzotti, S., & Hyndman, R. D. (2002). Yakutat collision and strain transfer across the northern Canadian Cordillera. *Geology*, *30*(6), 495–498. https://doi.org/10.1130/0091-7613(2002)030

Mazzotti, S., Leonard, L. J., Hyndman, R. D., & Cassidy, J. F. (2008). Tectonics, dynamics, and seismic Hazard in the Canada-Alaska Cordillera. *Geophysical Monograph Series*, 297–319. https://doi.org/10.1029/179gm17

McConeghy, J., Flesch, L., & Elliott, J. (2022). Investigating the effect of mantle flow and viscosity structure on surface velocities in Alaska using 3-D geodynamic models. *Journal of Geophysical Research: Solid Earth*, *127*(10). https://doi.org/10.1029/2022jb024704

Miller, E. L., & Hudson, T. L. (1991). Mid-cretaceous extensional fragmentation of a Jurassic-early cretaceous compressional orogen, Alaska. *Tectonics*, *10*(4), 781–796. https://doi.org/10.1029/91tc00044

Miller, M. S., & Moresi, L. (2018). Mapping the Alaskan Moho. *Seismological Research Letters*, *89*(6), 2430–2436. https://doi.org/10.1785/0220180222

Montagner, J., & Nataf, H. (1988). Vectorial tomography—I. Theory. *Geophysical Journal*, *94*(2), 295–307. https://doi.org/10.1111/j.1365-246x.1988.tb05903.x

Montagner, J., & Tanimoto, T. (1991). Global upper mantle tomography of seismic velocities and anisotropies. *Journal of Geophysical Research*, *96*(B12), 20337–20351. https://doi.org/10.1029/91jb01890

Moore, T. E., & Box, S. E. (2016). Age, distribution and style of deformation in Alaska north of 60°N: Implications for assembly of Alaska. *Tectonophysics*, *691*, 133–170. https://doi.org/10.1016/j.tecto.2016.06.025

Moore, T. E., O'Sullivan, P. B., Potter, C. J., & Donelick, R. A. (2015). Provenance and detrital zircon geochronologic evolution of lower Brookian foreland basin deposits of the Western Brooks Range, Alaska, and implications for early Brookian tectonism. *Geosphere*, *11*(1), 93–122. https://doi.org/10.1130/ges01043.1

Moore, T. E., Wallace, W. K., Bird, K. J., Karl, S. M., Mull, C. G., & Dillon, J. T. (1994). The geology of North America (pp. 49–140). https://doi.org/10.1130/dnag-gna-g1.49

Moschetti, M. P., Ritzwoller, M. H., Lin, F., & Yang, Y. (2010). Seismic evidence for widespread Western-US deep-crustal deformation caused by extension. *Nature*, *464*(7290), 885–889. https://doi.org/10.1038/nature08951

O'Brien, T. M., Miller, E. L., Pease, V., Hayden, L. A., Fisher, C. M., Hourigan, J. K., & Vervoort, J. D. (2018). Provenance, U-Pb detrital zircon geochronology, Hf isotopic analyses, and Cr-spinel geochemistry of the northeast Yukon-Koyukuk Basin: Implications for interior basin development and sedimentation in Alaska. *GSA Bulletin*, *130*(5–6), 825–847. https://doi.org/10.1130/b31825.1

Ozacar, A. A., & Zandt, G. (2004). Crustal seismic anisotropy in central Tibet: Implications for deformational style and flow in the crust. *Geophysical Research Letters*, *31*(23). https://doi.org/10.1029/2004gl021096

Patton, W. W. (1973). *Reconnaissance geology of the northern Yukon-Koyukuk province, Alaska (Professional paper)* (p. 774-A). US Geological Survey.

Pavlis, T. L., Sisson, V. B., Foster, H. L., Nokleberg, W. J., & Plafker, G. (1993). Mid-cretaceous extensional tectonics of the Yukon-Tanana terrane, trans-Alaska crustal transect (TACT), east-central Alaska. *Tectonics*, *12*(1), 103–122. https://doi.org/10.1029/92tc00860

Pavlis, T. L., Sisson, V. B., & Roeske, S. M. (2003). Geology of a transpressional orogen developed during ridge-trench interaction along the North Pacific margin. https://doi.org/10.1130/0-8137-2371-x.191

Plafker, G., Moore, J. C., & Winkler, G. R. (1994). Geology of the southern Alaska margin.

Redfield, T. F., Scholl, D. W., Fitzgerald, P. G., & Beck, M. E. (2007). Escape tectonics and the extrusion of Alaska: Past, present, and future. *Geology*, *35*(11), 1039–1042. https://doi.org/10.1130/g23799a.1

Savage, M. K. (1999). Seismic anisotropy and mantle deformation: What have we learned from shear wave splitting? *Reviews of Geophysics*, *37*(1), 65–106. https://doi.org/10.1029/98rg02075

Schulte-Pelkum, V., Caine, J. S., Jones, J. V., & Becker, T. W. (2020). Imaging the tectonic grain of the northern Cordillera orogen using transportable array receiver functions. *Seismological Research Letters*, *91*(6), 3086–3105. https://doi.org/10.1785/0220200182

Shapiro, N. M., & Campillo, M. (2004). Emergence of broadband Rayleigh waves from correlations of the ambient seismic noise. *Geophysical Research Letters*, *31*(7). https://doi.org/10.1029/2004gl019491

Shen, W., & Ritzwoller, M. H. (2016). Crustal and uppermost mantle structure beneath the United States. *Journal of Geophysical Research: Solid Earth*, *121*(6), 4306–4342. https://doi.org/10.1002/2016JB012887

Sherrington, H. F., Zandt, G., & Frederiksen, A. (2004). Crustal fabric in the Tibetan Plateau based on waveform inversions for seismic anisotropy parameters. *Journal of Geophysical Research*, *109*(B2). https://doi.org/10.1029/2002jb002345

Silwal, V., Tape, C., & Lomax, A. (2018). Crustal earthquakes in the Cook inlet and Susitna region of southern Alaska. *Tectonophysics*, *745*, 245–263. https://doi.org/10.1016/j.tecto.2018.08.013

Smith, M. L., & Dahlen, F. A. (1973). The azimuthal dependence of love and Rayleigh wave propagation in a slightly anisotropic medium. *Journal of Geophysical Research*, *78*(17), 3321–3333. https://doi.org/10.1029/JB078i017p03321

Wang, Y., & Tape, C. (2014). Seismic velocity structure and anisotropy of the Alaska subduction zone based on surface wave tomography. *Journal of Geophysical Research: Solid Earth*, *119*(12), 8845–8865. https://doi.org/10.1002/2014jb011438

Weiss, T., Siegesmund, S., Rabbel, W., Bohlen, T., & Pohl, M. (1999). Seismic exploration of the deep continental crust. *Methods and Concepts of DEKORP and Accompanying Projects*, 97–122. https://doi.org/10.1007/978-3-0348-8670-3_6

Xie, J., Ritzwoller, M. H., Brownlee, S. J., & Hacker, B. R. (2015). Inferring the oriented elastic tensor from surface wave observations: Preliminary application across the Western United States. *Geophysical Journal International*, *201*(2), 996–1021. https://doi.org/10.1093/gji/ggv054

Xie, J., Ritzwoller, M. H., Shen, W., & Wang, W. (2017). Crustal anisotropy across eastern Tibet and surroundings modeled as a depth-dependent tilted hexagonally symmetric medium. *Geophysical Journal International*, ggx004. https://doi.org/10.1093/gji/ggx004

Xie, J., Ritzwoller, M. H., Shen, W., Yang, Y., Zheng, Y., & Zhou, L. (2013). Crustal radial anisotropy across eastern Tibet and the Western Yangtze Craton. *Journal of Geophysical Research: Solid Earth*, *118*(8), 4226–4252. https://doi.org/10.1002/jgrb.50296

Zhang, Y., Li, A., & Hu, H. (2019). Crustal structure in Alaska from receiver function analysis. *Geophysical Research Letters*, *46*(3), 1284–1292. https://doi.org/10.1029/2018gl081011

Zinke, J. C., & Zoback, M. D. (2000). Structure-related and stress-induced shear-wave velocity anisotropy: Observations from microearthquakes near the Calaveras fault in central California. *Bulletin of the Seismological Society of America*, *90*(5), 1305–1312. https://doi.org/10.1785/0119990099